Multi-Mode Attractors and Spatio-Temporal Canards

Theodore Vo[1], Richard Bertram[2], and Tasso J. Kaper[3]

[1]School of Mathematics, Monash University, Clayton, Victoria 3800, Australia
[2]Department of Mathematics and Programs in Neuroscience and Molecular Biophysics, Florida State University, Tallahassee, FL 32306, USA
[3]Department of Mathematics and Statistics, Boston University, Boston, MA 02215, USA

March 27, 2020

Abstract

In this article, we report the numerical discovery of multi-mode attractors for reaction-diffusion systems in which the kinetics feature slow/fast dynamics. Multi-mode attractors (MMAs) are a class of attractors in which different regions of the spatial domain exhibit different modes of (temporal) oscillation. These modes include spiking modes, bursting modes of many different types with s small-amplitude oscillations at the end of each burst event, as well as alternating modes in which various sequences of spiking and bursting are exhibited in alternation. We present the numerical discovery of MMAs in the context of a spatially-extended pituitary cell model with diffusive coupling and a spatially inhomogeneous applied current. We demonstrate that the MMAs are robust, occurring on large open parameter sets and for a variety of biophysically-relevant spatially-inhomogeneous currents, including Gaussian and mollified step profiles. Also, we provide evidence that the MMAs exhibit new types of maximal spatio-temporal canards. These lie in the transition intervals between adjacent regions in which the MMA exhibits distinct modes of oscillation, and they are necessary for the smooth and gradual transitions between bursting and spiking, as well as between bursting modes with different numbers of small oscillations. Furthermore, we study how the structures of the MMAs change as the amplitude of the diffusivity decreases and the PDE model limits on a family of uncoupled ODEs, one for each point in the domain. Also, we show that the MMAs, which are spatially non-uniform, can coexist in the reaction-diffusion system with other types of attractors which are spatially-uniform. Finally, we report that the MMAs discovered here are also present in numerical simulations of other reaction-diffusion systems, especially those that arise in neural and cardiac models.

Keywords multi-mode attractor, spatio-temporal canard, mixed-mode oscillation, reaction-diffusion, diffusive coupling, bursting, spiking, pituitary lactotroph

Dedication This new class of patterns is presented in honour of Ehud Meron's 60^{th} birthday.

1 Introduction

We report the numerical discovery of *multi-mode attractors* (MMAs) of spatially extended systems in which the kinetics feature a slow/fast structure. The MMAs are a class of attractors of reaction-diffusion systems in which different parts of the spatial domain exhibit different modes of oscillation, and they may be periodic or quasi-periodic in time. The spatial transition intervals between the different modes of activity exhibit spatio-temporal canard dynamics.

A representative MMA, discovered in a spatially extended model for the electrical activity in pituitary lactotrophs/somatotrophs with spatially inhomogeneous applied current and diffusive

coupling, is shown in Fig. 1. The MMA consists of three modes, each of which occurs in a different region of the spatial domain: one in which the attractor is in the spiking mode, one in which the attractor is in a pseudo-plateau bursting mode with one small oscillation per burst event, and a region in which the attractor is in an alternator mode, alternatively exhibiting spikes and pseudo-plateau bursts. Since the mode of oscillation in this attractor differs across the three regions, we refer to this as a 3-mode *multi-mode attractor*.

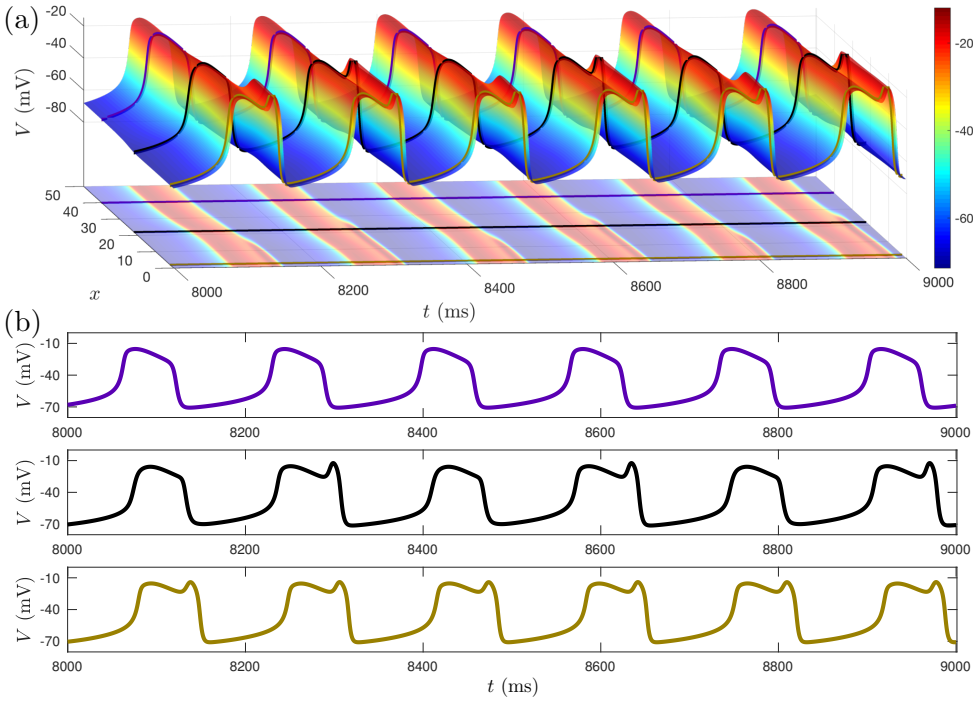

Figure 1: A representative 3-mode MMA, which is period-2 in time, in a spatially extended model for the electrical activity in pituitary somatotrophs/lactotrophs with spatially heterogeneous applied current and diffusive coupling. (a) Voltage dynamics of the attractor. In the inner region, the attractor exhibits 1^1 pseudo-plateau bursts (olive curve; $x = 2$). In the outer region, the attractor exhibits 1^0 spiking (purple curve; $x = 40$). Between the spiking and bursting regions, there is a region in which the temporal dynamics alternate between spiking and bursting (black curve; $x = 22$). The voltage heat map has been projected into the (x, t) plane; active phases are indicated by the red bands and silent phases by the blue bands. (b) Time series for representative x values in each of the spiking (top), alternator (middle), and bursting (bottom) regions.

1.1 Spatially Extended Pituitary Cell Model

In an *in vivo* setting, somatotrophs and, likely, lactotrophs (which secrete growth hormone and prolactin, respectively) form networks of coupled cells where the coupling is through gap junctions [5]. This provides nearest-neighbor diffusive electrical coupling between the cells that, in the continuum limit, is described by the diffusion operator. In this limit, and for a linear network of coupled cells, the partial differential equations (PDEs) have the form

$$\begin{aligned} C_m \frac{\partial V}{\partial t} &= I_{\text{app}}(x) - I_{\text{ion}} + D\frac{\partial^2 V}{\partial x^2}, \\ \frac{ds}{dt} &= \frac{s_\infty(V) - s}{\tau_s}, \quad s = n, e, \end{aligned} \tag{1.1}$$

where $V(x,t)$ is the membrane potential at position x at time t, and $s(x,t)$ represents the two (slow) gating variables for the ionic currents, I_{ion}, intrinsic to the cells (see Appendix A.1). The applied current, $I_{\text{app}}(x)$, is spatially dependent, reflecting the fact that different cells in the network are exposed to different levels of neurohormones that serve to activate or inhibit the cells' electrical activity. For most of this article (except in Section 8), we set $I_{\text{app}}(x)$ to be a Gaussian

$$I_{\text{app}}(x) = I_{\text{base}} + (I_{\max} - I_{\text{base}}) \exp\left(-\frac{x^2}{4\sigma}\right), \tag{1.2}$$

where I_{base} is the baseline applied current, $I_{\max}$ is the maximal applied current, and σ is the half-width. This is partially motivated by the fact that experiments show portions of the brain are inhomogeneous media, with localized synaptic currents. For example, auditory cortex EEG data in certain primates exhibits localized currents (see fig. 2 of [25]). In these experiments, a multi-electrode array was placed to span -and sample from- all layers of the auditory cortex. It was reported that the locally generated intracortical synaptic currents exhibited localized maxima at certain spatial locations, including in the supragranular layers and the granular layer of the cortex. While the exact functional form of these synaptic currents is unknown, as yet, a Gaussian profile provides a good first qualitative model for these tapered peaks.

The kinetics of the reaction-diffusion system (1.1) are described by the one-parameter family of *x-dependent ordinary differential equations* (ODEs),

$$\begin{aligned} C_m \frac{dV}{dt} &= I_{\text{app}}(x) - I_{\text{ion}}, \\ \frac{ds}{dt} &= \frac{s_\infty(V) - n}{\tau_s}, \quad s = n, e, \end{aligned} \tag{1.3}$$

and are based on a minimal model for the electrical activity in pituitary cells [39]. The family of x-dependent ODEs is obtained from (1.1) by setting $D = 0$ (so that all cells are decoupled), and is a useful auxiliary system for studying the dynamics of the PDE (1.1). A key feature of the kinetics is that it evolves over multiple timescales, with fast voltage dynamics and slow gating dynamics. Geometric singular perturbation techniques [14, 20, 30] have been used to leverage the slow/fast structure of such systems and hence uncover the origins and properties of the pseudo-plateau bursting that evokes hormone release. In the setting of pituitary lactotrophs, the pseudo-plateau bursting is a canard-induced mixed-mode oscillation [37, 41]. The small-amplitude oscillations (SAOs) of a 1^s attractor arise from local canard dynamics around a folded node singularity [11, 36, 43], and the large-amplitude oscillations are of relaxation type. There is a rich and robust family of $(1^s)^k(1^{s+1})^\ell$ alternator states between the 1^s and 1^{s+1} states, and these are shown over a wide range of (g_K, g_A) parameter space in Figures 2, 3, and 5 of [42]. More specifically, the folded node gives rise to a family of maximal canards, γ_k for $k = 0, 1, \ldots, s_{\max}$, each pair of which delimits subsets of the phase space with different numbers of SAOs. The s SAOs of the 1^s attractor occur because the orbit is periodically re-injected into the sector of phase space enclosed by the $(s-1)^{\text{th}}$ and s^{th} maximal canards. Consequently, bifurcations of the pseudo-plateau bursts are often related to bifurcations of the maximal canards (see Appendix A.2).

1.2 Main Contributions

In reporting on the discovery of the MMAs in the context of the continuum pituitary somatatroph/lactotroph model (1.1) with spatially inhomogeneous applied current and diffusive coupling, we present the following main contributions. First, we establish the existence of a base case 3-mode

MMA which exhibits three regions, each with its own distinct mode of oscillation, including a central region in which the cells oscillate in a 1^1 bursting mode, a middle region in which the cells exhibit a $1^1 1^0$ alternator mode, and an outer region in which the cells are in the 1^0 spiking mode. This base case 3-mode MMA is created by a Gaussian applied current in (1.1), which models a spatially-localized current. Cells in the center of the line receive a larger applied current than cells toward the end of the line, and as a result cells in the central region exhibit bursting, whereas cells toward the outer end of the line are in the spiking mode. We show that the key properties of the Gaussian applied current, including the base current level, the maximum current amplitude, and the half-width, determine which cells exhibit which mode. We also use various diagnostics, including the action potential duration, to study the dynamics and geometry of this base case 3-mode MMA.

Next, in the context of this base case 3-mode MMA, we identify the new maximal spatio-temporal canards that exist within MMAs in the transition intervals between regions of distinct modes. In particular, we show that the time traces at key spatial locations in the transition intervals between adjacent modes of the MMAs exhibit features that are highly similar to the maximal canards known to exist in the single-cell ODE model [42]. These spatio-temporal canards must exist in the transition intervals between adjacent regions with distinct modes in order for the number of SAOs to transition continuously in space along the cell line. In particular, we find that maximal spatio-temporal canards exist in time traces taken at key locations in the transition intervals between adjacent regions with a 1^1 bursting mode and a $1^1 1^0$ alternator mode, as well as in the intervals between adjacent alternator modes and the 1^0 spiking mode. For all of these different types of MMAs, we find that the maximal spatio-temporal canards mediate the loss (or gain) of SAOs in the active phase.

Then, we illustrate the richness of the n-mode MMAs of (1.1) by providing examples with $n = 4$ and 5, as well as by describing a general method for generating n-mode MMAs of different types. We show that there are n-mode MMAs which exhibit several different types of $(1^1)^k(1^0)^\ell$ alternator modes for positive integers k and ℓ, in addition to the basic 1^1 bursting and 1^0 spiking modes. Also, we show that there are n-mode MMAs in which the modes consist of 1^s bursting, with s SAOs at the end of each burst, for various positive integers s, providing a rich tapestry of patterns. For these MMAs in which adjacent regions have 1^{s+1} and 1^s bursting modes, maximal spatio-temporal canards also exist in the time traces at key locations x in the transition intervals, and also here they mediate the loss (or gain) of SAOs. Throughout this study of general n-mode MMAs, we show that for understanding how the distinct modes of oscillation are created in different regions along the line of cells, it is exceptionally useful to have the detailed available knowledge from the single-cell models [41, 42] about the distinct 1^0 spiking attractors, 1^s bursting attractors and $(1^{s+1})^k(1^s)^\ell$ alternating attractors, as well as about the large regimes in parameter space for which they exist, and their bifurcations.

Having established the existence and fundamental properties of these different types of general n-mode MMAs, we turn to a study of their robustness in parameter space, establishing their ubiquity as attractors of the PDE (1.1). This is done primarily in the context of the base case 3-mode MMA. We show that this MMA (and other MMAs) exist in large open sets of parameter space and that they are robust with respect to the main control parameters of the spatially-localized Gaussian currents. Moreover, we demonstrate that MMAs can be generated by other types of spatially-dependent applied currents, not just the spatially-localized Gaussian currents used throughout most of this study. Specifically, MMAs are also generated by biophysically-relevant step function type currents in which half the cell line receives one level of applied current and the other half receives a different level of applied current, mollified bump function currents, and inverse bump function currents, as well as by spatially-dependent maximal conductivities. For each of these, detailed knowledge

available about parameter dependence in the single-cell model is useful for understanding how the various MMAs are generated by these different types of spatially-dependent currents.

Furthermore, for the PDE (1.1), we carry out a study of the effect of the magnitude of the spatial coupling. This includes a comparison, over a range of D values, between the geometry and dynamical structures of the n-mode MMAs of the PDE (1.1) and the structures and invariant manifolds of the family of x-dependent ODEs (1.3). Also, it includes some analysis of how the dynamics of the MMAs change in the limit in which $D \to 0$, in which the PDE (1.1) limits on the family of x-dependent ODEs (1.3).

Finally, we demonstrate that (1.1) is bistable, showing that there is also a single-mode 1^1 bursting attractor of the PDE that coexists with the various n-mode MMAs of (1.1) reported on here in each of the respective regimes of parameter space over which these n-mode MMAs are found. Moreover, we briefly show that MMAs also exist in three other reaction-diffusion models, including in a diffusive forced van der Pol PDE, in a biophysically detailed rabbit heart tissue model that generates early afterdepolarizations, and in a simplified model for the electrical activity in cardiomyocytes.

1.3 The new MMAs and larger context of spatio-temporal canards

In this section, we describe how the new phenomenon of MMAs for reaction-diffusion PDEs fits into the larger context of the nascent literature on spatio-temporal canards.

Some of the earliest instances of canards in PDEs were identified as traveling wave solutions of the PDE, and they were constructed as homoclinic and heteroclinic connections with canard segments in the traveling wave ODE. Hence, these first occurrences follow directly from classical theory of canards for ODEs. Such constructions can be found, for instance, in a spruce budworm reaction-diffusion population model [8]; in a scalar viscous conservation law with nonlinear source (i.e., advection-reaction-diffusion equation) as often occurs in nozzle flow problems [19]; and in combustion waves for an autocatalytic reaction where canard solutions of the underlying ODE separate the slow combustion regime from the explosive one [33]. Jump and entropy conditions for shocks in coupled advection-reaction-diffusion equations were formulated in terms of canards [45] in the corresponding traveling wave ODE. These results were applied to shock-fronted traveling waves in models of wound healing angiogenesis [18] and (melanoma) tumor invasion [17]. Moreover, shock solutions that arise in the steady spherically symmetric outflow from the surface of a star were identified as canard trajectories in the ODE for the density as a function of the radial variable, allowing for an explanation of the location of the shock and its sensitivity to parameters [9].

More recently, non-traveling wave canard-type phenomena have been investigated in reaction-diffusion systems. For instance, diffusion-induced instabilities of small-amplitude phase waves leading to the initiation of large-amplitude trigger waves were studied in a one-dimensional (1D), two-component model of the Belousov-Zhabotinsky reaction [6]. There, it was demonstrated that the trigger waves could be initiated at any point in the excitable medium provided the kinetics were sufficiently close to a canard point. Rigorous studies of spatio-temporal bifurcation delays associated with canard solutions in singularly perturbed parabolic PDEs have also been carried out for several configurations. For example, the subcases of transcritical and pitchfork bifurcations of the fast subsystem kinetics were treated in [27], and the case of turning points in the linear part of the kinetics was studied in [10]. For the reaction-diffusion equations with turning points, sub- and super-solutions were constructed analytically to prove that there are canard solutions of the PDE which stay near repelling states for long times. Moreover, it was established that for sufficiently small diffusivities, the duration of the canard segments can be spatially inhomogeneous.

The next major breakthrough in the *spatio-temporal canard* phenomenon occurred in a deter-

ministic Amari-type neural field model [3, 15]. In this system, coherent structures in which the spatial patterns, in their entireties, display temporal canard behaviour were identified and described for generic choices of firing rates and synaptic kernels. Moreover, the existence of complex spatiotemporal patterns containing canard segments was reported, and a theory for the classification of such spatio-temporal canards was derived from interfacial dynamics. Both canards of folded node and folded saddle types were demonstrated, paving the way for a systematic study of spatio-temporal MMOs.

Further progress in spatio-temporal canards came in the context of transitions from convective to absolute instabilities in advection-reaction-diffusion systems of the type encountered in shear flow problems [4]. It was demonstrated that for Dirichlet boundary conditions, the system evolves to a trivial steady state. However, when the inlet boundary condition is taken to be a non-zero constant, η, the steady state to which the system evolves exhibits extremely sensitive dependence on η. This parameter sensitivity was explained by canard segments of the spatial boundary value problem for the steady states of the PDE.

The MMAs presented in this article contain completely new types of spatio-temporal canards. In particular, we show that the time traces at certain values of x, located in the transition intervals between regions of distinct and adjacent modes of the MMA, are maximal spatio-temporal canards. They mediate the transitions between adjacent 1^s and 1^{s+1} regions in the MMAs. Indeed, for the time courses to vary continuously from a 1^s mode to a 1^{s+1} mode as one steps through the cell locations x in the transition intervals, there must be (at least) one cell location at which the new small-amplitude oscillation is first created. In this manner, certain fundamental maximal canards from the family (1.3) of x-dependent ODEs persist in the PDE with diffusive coupling.

1.4 Relation to Chimera States for Coupled Oscillators

Chimera states were discovered in two models of densely and uniformly distributed identical oscillators subject to finite-range nonlocal coupling, including a non-locally coupled complex Ginzburg-Landau equation, by Kuramoto and Battogtokh [24, 23]. In chimera states, there are coexisting domains of mutually synchronized oscillators and domains of desynchronized oscillators with distributed frequencies. In the former, the oscillators are coherent and phase-locked, and the states may be either stationary or propagate. In contrast, in the latter, the oscillators are decoherent, and their phases drift relative to each other and to the phase-locked oscillators [24, 23, 34, 2, 1, 28].

Chimera states have been discovered experimentally, [16, 38], and are the subject of intensive further study both theoretically and experimentally, see for example [29] for a recent review and [46]. Moreover, chimera states have also been found to occur due solely to global coupling (i.e., without the non-local coupling originally thought necessary) in an array of coupled Stuart-Landau oscillators and in a modified complex Ginzburg-Landau equation [32].

In a generalized sense, MMAs have some qualitative features in common with chimera states in coupled oscillators and in nonlinear reaction-diffusion equations. In the MMAs, as we show here, there are distinct modes of coherent, phase-locked oscillation coexisting on different regions; there are parameter regimes in which the coherent states are stationary (as studied here) and regimes in which they propagate into other coherent states; and, there is bistability with a homogeneous bursting attractor, just as there is often bistability of an asynchronous chimera state with a spatially-symmetric synchronous state.

However, in the MMAs studied here, each of the regions contain distinct modes of synchronous oscillation, and the oscillations are all of the types generated by folded singularities, unlike the types of coherent states studied to date in chimera states. Of equal import, in MMAs, the transition intervals between different modes in adjacent regions exhibit maximal spatio-temporal canards, a

feature which does not appear to have been observed yet along the boundaries of different domains in chimera states. Furthermore, the PDE (1.1) and the PDEs in Section 9.3 have purely local coupling, so that there is no need to have non-local or global coupling for the MMAs. Finally, for small D, close to the limit in which the PDE (1.1) approaches the family of x-dependent ODEs, the alternator regions exhibit propagating fronts, hence also these are coherent, in contrast with the incoherence observed in certain domains of chimera states.

1.5 Outline of the Article

This article is organized as follows. In Section 2, the geometric structures and dynamics of the three modes in the base case 3-mode MMA are presented in detail, along with the maximal spatial temporal canards in the transition intervals. Section 3 contains the presentation and analysis of the general n-mode MMAs. In Section 4, the robustness of n-mode MMAs is illustrated.

Next, in Section 5, we present the comparison of the geometric structures of the PDE (1.1) and the family of x-dependent ODEs (1.3), illustrating this in detail for the base case 3-mode MMA. Then, in Section 6, there is an examination of how the magnitude of the spatial coupling affects the geometric structure and dynamics of the MMAs, again focusing on the base case 3-mode MMA.

We follow in Section 7 by presenting the bistability results for the PDE (1.1). In Section 8, the different forms of applied currents are examined, to provide further evidence of how spatial inhomogeneity induces the attractors of (1.1) to be of multi-mode type. Finally, in Section 9, we summarize our main results, provide a (partial) list of the many open questions raised by this discovery of MMAs, and briefly report on the existence of MMAs in three other models.

2 A base case 3-mode MMA with spiking, bursting, and alternator regions

In this section, we introduce a base case 3-mode MMA of system (1.1) with $D = 1$, which consists of three regions, each with its own distinct mode of behaviour (Fig. 2(a)). In the bursting region ($0 \leq x \lesssim 9$), the attractor is in a 1^1 bursting mode (where the bursts have one SAO at the end of each event and are known as pseudo-plateau bursts). A representative time series of the voltage, $V(x,t)$, in the bursting region is shown in the top panel of Fig. 2(b). Next, in the alternator region ($16 \lesssim x \lesssim 22$), the attractor is in the alternator mode with the voltage time series switching between 1^1 bursts and 1^0 spikes (Fig. 2(b), middle). In the spiking region ($27 \lesssim x \leq 50$), the attractor is in the spiking mode where it exhibits 1^0 spikes (Fig. 2(b), bottom).

In each of these regions, the solution is time-periodic. In the alternator region, the period is approximately 336 ms and corresponds to the duration of a pair of spike and burst events, whereas in the spiking and bursting regions, the period is approximately half that. Therefore, in this base case, the entire 3-mode MMA is period-2, with a total period of approximately 336 ms corresponding to two successive events.

For a cell at a fixed location x, the action potential duration (APD) is defined to be the amount of time the cell spends in the active phase (i.e., with $V(x,t) > -45$ mV). More precisely, for each x we consider the sets

$$\Sigma_x^+ = \left\{(t,V,n,e) : V = -45 \text{ mV and } \tfrac{\partial V}{\partial t} > 0\right\},$$
$$\Sigma_x^- = \left\{(t,V,n,e) : V = -45 \text{ mV and } \tfrac{\partial V}{\partial t} < 0\right\},$$

of points at which the voltage is at the threshold (set here at -45 mV) and the solutions pass

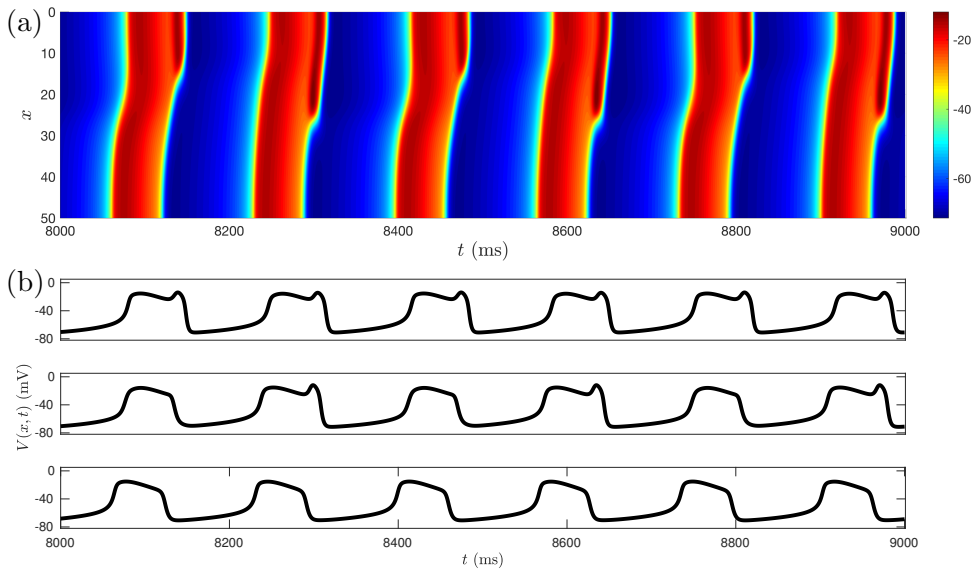

Figure 2: Steady state dynamics of the voltage, $V(x,t)$, of the MMA of (1.1) with $D = 1$, $\alpha = 10, \beta = 90$ and $p = 0.4$, corresponding to $I_{\text{base}} \approx -0.0058$ mA, $I_{\max} \approx 0.9033$ mA and $\sigma \approx 97.296$. (See Section 4 for interpretation of the control parameters α, β and p in terms of $I_{\text{base}}, I_{\max}$ and σ.) The initial conditions were normalized as described below. (a) Contour plot of the voltage with blue corresponding to hyperpolarization and red corresponding to depolarization. The dark wine red ledges in the bands of depolarization correspond to SAOs. (b) Time series of $V(x,t)$ at representative values of x in the 1^1 bursting region ($x = 8$; top), $1^0 1^1$ alternator region ($x = 20$; middle), and 1^0 spiking region ($x = 35$; bottom). (The results are only shown on the spatial domain [0,50], due to the symmetry.)

through the threshold with increasing and decreasing voltage, respectively, and construct the map

$$\Pi_x^A : \Sigma_x^+ \to \Sigma_x^-$$

to measure the duration of the active phase (Fig. 3(a) and (b)). Thus, the APD is the first return time to the voltage threshold, as measured by Π_x^A. These APD measurements vary as functions of x, due to the nonlinearities in the system and the spatial dependences of the attractors.

The APD profile for the base case 3-mode MMA shown in Fig. 2 is presented in Fig. 3(c) (blue diamonds and blue circles). In the bursting region ($0 \leq x \lesssim 9$), the APD profile (blue diamonds) of the MMA has two branches, which are close to each other (Fig. 3(c), near $x = 0$). In the alternator region ($16 \lesssim x \lesssim 22$), the upper branch (blue diamonds) has longer APD corresponding to the 1^1 bursting, which reflects the longer return time (on account of the small oscillation) of the map Π_x^A between the sections Σ_x^+ and Σ_x^- (recall Fig. 3(a) and (b)). The lower branch (blue circles) has shorter APD corresponding to the 1^0 spiking, which reflects the shorter return time of the solution (as measured by Π_x^A) from Σ_x^+ to Σ_x^-. The third region is the spiking region ($27 \lesssim x \leq 50$).

In between adjacent regions of the base case 3-mode MMA, there are transition intervals over which the structure of the MMA transitions from one mode to another. The first transition interval is $9 \lesssim x \lesssim 16$. Here, there is a transition in space from the bursting mode to the alternator mode. We examine the time series of the attractor sampled at different values of x (Fig. 4). There is a location x ($x \approx 9$) at which the amplitudes of the SAOs in the odd bursts reach a maximum (Fig. 4(b)). This marks the right edge of the bursting region and the left edge of this first transition interval. It corresponds to the time series of a maximal canard in the x-dependent ODE (1.3). Then, as one examines the voltage time traces of the MMA for $x \gtrsim 9$, the amplitudes of the SAOs in the

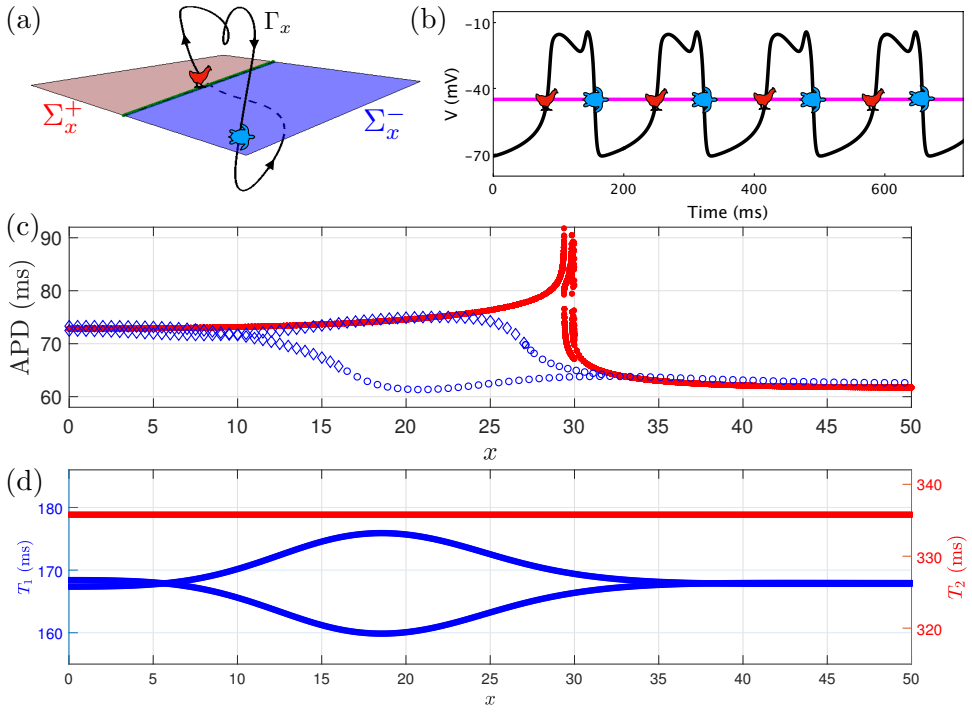

Figure 3: Illustration of some useful diagnostics of the base case 3-mode MMA, with the same parameters as in Fig. 2. (a) For each $x \in [0, L]$, the time course of the attractor at that location x is shown as the black curve Γ_x in the (V, n, e) space (here $x = 5$ for illustration). For each x, the map Π_x^A is the map from the point (red chicken) at which Γ_x crosses the section Σ_x^+ (red surface) to the point (blue turtle) at which Γ_x crosses the section Σ_x^- (blue surface). (b) For each x, the APD is the length of time between the red chicken and the blue turtle. (c) The APD profiles as functions of x for the 3-mode MMA (blue) of the PDE (1.1), and for the limit cycle attractors (red) of the family of x-dependent ODEs (1.3). In the blue APD profiles, a burst or spike event is indicated by an open diamond or circle, respectively. The spike/burst boundaries occur at the inflection points. (d) First full return time (blue curves) measured by the composite map $\Pi_x^S \circ \Pi_x^A$ (see text), and second full return times (red curve) measured by the map $\left(\Pi_x^S \circ \Pi_x^A\right)^2$, which indicates that the 3-mode MMA is a time-periodic solution of (1.1) with period of approximately 336 ms. Here, and in Figs. 6, 7, 13, and 16, the symbols are chosen arbitrarily; there is no significance attached to the particular animals.

odd bursts of the attractor decrease and go below those of the single-mode 1^1 burster (Figs. 4(c)–(e), $x \approx 13, 14$ and $x \approx 15$). Finally, once one reaches $x \approx 16$, the odd burst events no longer have SAOs. This value of x marks the right endpoint of this first transition interval, and for $x \gtrsim 16$ the attractor is in the alternator mode (Fig. 4(f)). In this manner, over the span of this first transition interval, the odd bursts have become the 1^0 spiking events, and the even bursts have remained as 1^1 events. Moreover, the APD provides a clear diagnostic about this loss of the SAO in the odd burst events, because there is an inflection point at $x \approx 16$ on the lower branch, exactly where the SAO disappears.

The spatial derivative of the APD profile provides further insight; Fig. 4(g) shows the spatial derivative of the lower (blue) branch of the APD profile from Fig. 3(c), corresponding to the odd burst events. There is a minimum at $x \approx 16$ with relatively sharp slope. This corresponds to the inflection point of the APD profile where the diamonds transition to circles, see Fig. 3(c), and marks the boundary between the first transition interval and the alternator mode.

Next, we describe the transition from the alternator region to the spiking region ($22 \lesssim x \lesssim 27$). There is a value of x ($x \approx 22$) for which the SAOs of the even bursts have maximal amplitude.

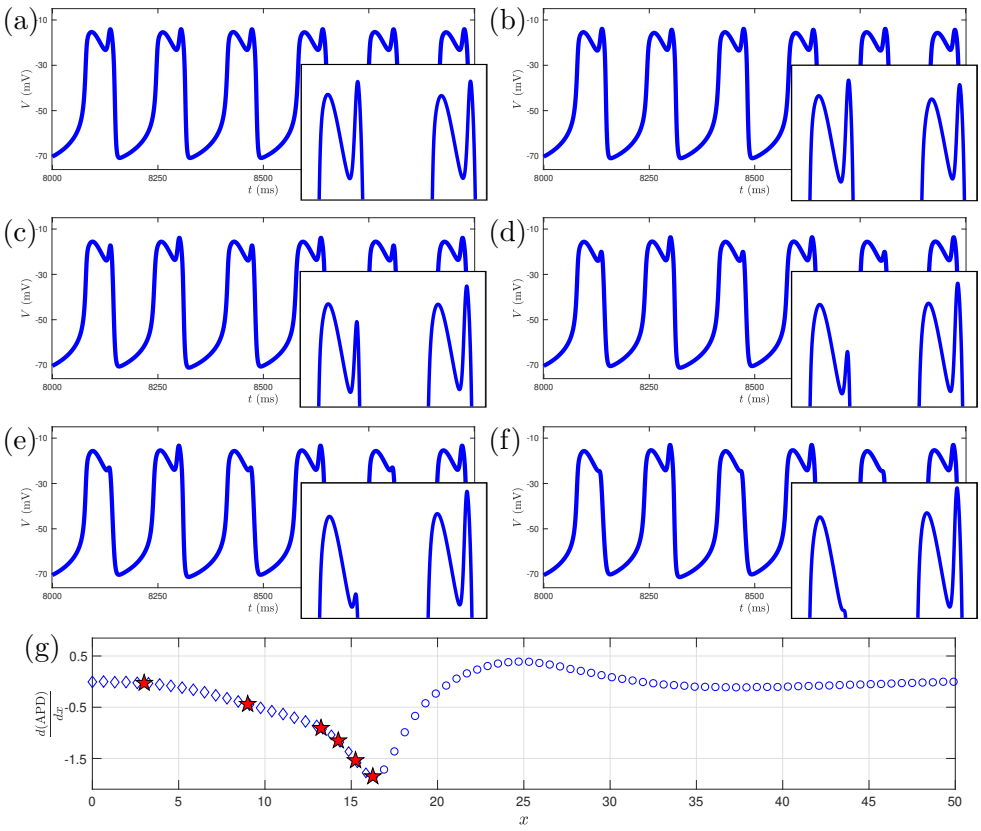

Figure 4: Maximal spatio-temporal canards mediate the transition from the bursting mode to the alternator mode for the base case 3-mode MMA. Time series are shown for (a) $x = 3$, (b) $x = 9$, (c) $x = 13$, (d) $x = 14$, (e) $x = 15$ and (f) $x = 16$. These illustrate the loss of the SAO in the odd burst events due to the transition through a maximal spatio-temporal canard. (g) Spatial derivative of the lower APD profile from Fig. 3(c), corresponding to the odd burst events in the time series. There is a local minimum at $x \approx 16$ with relatively sharp spatial slope, corresponding to the inflection point in the APD profile.

This corresponds to a maximal spatio-temporal canard and is also where the upper APD branch in Fig. 3(c) attains its maximum. This marks the right boundary of the alternator region and the left edge of this second transition interval. As one examines time traces of the MMA for $x \gtrsim 22$, the even burst SAOs decrease in amplitude (Figs. 5(a)–(c)) and eventually disappear at $x \approx 27$ (Fig. 5(d)), corresponding to the right boundary of this second transition interval and the left edge of the spiking region. The spatial derivative of the APD profile for the even burst events (Fig. 5(e)) reveals that the inflection point is the boundary between this second transition interval and the spiking modes.

Having discussed the features of the APD profiles for the PDE in each of the three primary regions as well as in the transition intervals, we discuss how they compare to the APD measurements for the x-dependent ODEs (Fig. 3(c), red curves). First, the (red) APD profile for the attractors of (1.3) consists of a 1^0 spiking branch ($30 \leq x \leq 50$), a 1^1 bursting branch ($0 \leq x \lesssim 29.4$), and a region of $(1^1)^k(1^0)^\ell$ alternator branches ($29.4 \lesssim x < 30$). The transitions between the branches are mediated by maximal canards of (1.3), see Appendix A.2 or [42]. As shown in Fig. 3(c), for large segments of each of the three regions, the (blue) APD curves of the MMA are close to the (red) APD curves of the spiking attractors of (1.3). In particular, for most x ($0 \leq x \lesssim 8$) in the bursting region and for most x ($32 \lesssim x \leq 50$) in the spiking region, the difference in the APD

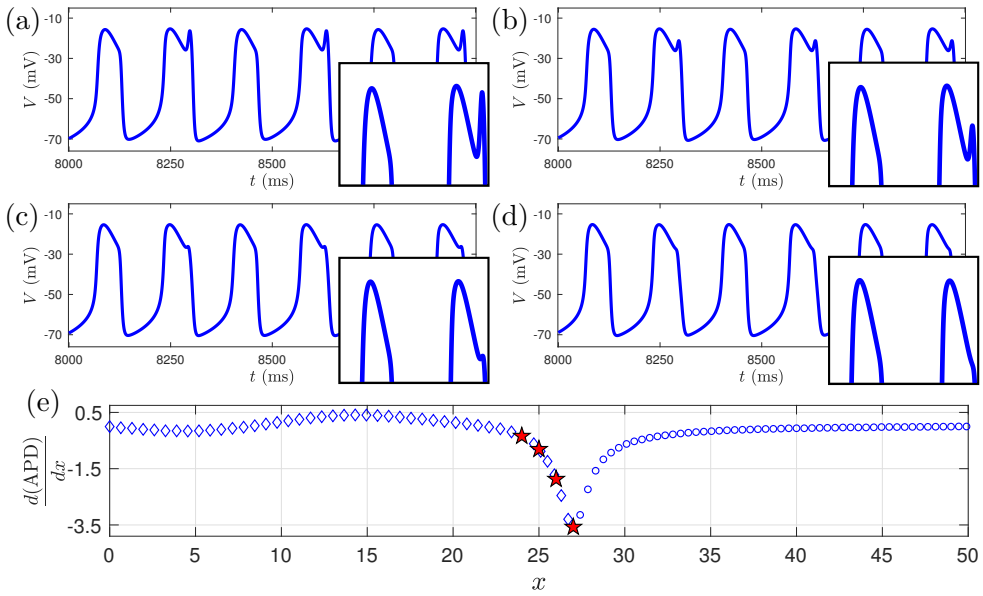

Figure 5: Maximal spatio-temporal canards mediate the transition from the alternator mode to the spiking mode for the base case 3-mode MMA. Time series for (a) $x = 24$, (b) $x = 25$, (c) $x = 26$, and (d) $x = 27$. Insets: zoom on the active phases of the last two events. These illustrate the loss of the SAO due to the transition through a maximal spatio-temporal canard. (e) Spatial derivative of the upper APD profile from Fig. 3(c), corresponding to the even events. The local minimum at $x \approx 27$ with relatively sharp spatial slope corresponds to the inflection point in the APD profile, and is the boundary between the alternator and spiking modes.

measurements between the MMA (blue) and the 1^0 and 1^1 attractors of the family of x-dependent ODEs (red) is less than 0.8 ms. Similarly, for most x ($17 \lesssim x \lesssim 22$) in the alternator region, the APD measurements for the burst events in the alternator mode of the PDE (upper, blue diamonds) are also within 0.8 ms of the APD measurements for the 1^1 bursting attractors of (1.3). The PDE and ODE measurements deviate from each other near where there is a loss or gain of a small oscillation in the active phase, corresponding either to a transition through a maximal canard of the family of x-dependent ODEs or through a spatio-temporal canard of the PDE. Thus, for $D = 1$, the MMA of the PDE preserves the spiking and bursting behaviour of the ODE, however, it stretches the alternator interval of (1.3) and only preserves the $1^1 1^0$ rhythms.

Finally, we observe for this base case 3-mode MMA that the APD profile shows that the entire attractor is a 2-periodic solution of (1.1). For each fixed x, we calculate the n^{th} return times, $T_n(x)$. More precisely, the first full return time, $T_1(x)$, measured from the composite map $\Pi_x^S \circ \Pi_x^A$, is the time taken for an orbit to complete one active phase and one silent phase, where Π_x^S is the map defined by

$$\Pi_x^S : \Sigma_x^- \to \Sigma_x^+.$$

Similarly, the second full return time, $T_2(x)$, measured from the composite map $\left(\Pi_x^S \circ \Pi_x^A\right)^2$, is the time taken for an orbit to complete two active phases and two silent phases, and so on. In terms of the contour plot in Fig. 2, $T_n(x)$ is the total horizontal width of n (active) red bands and n (silent) blue bands. The first and second full return times are shown in Fig. 3(d). The first full return profile (blue curves) shows the same qualitative information as the APD profile in Fig. 3(c). The second full return profile (red curve) is uniform in x. Thus, the base case 3-mode MMA is a 2-periodic solution in time of (1.1).

3 General n-mode MMAs

In this section, we present a series of n-mode MMAs with different types of alternators and with different types of 1^s burst events. First, in Section 3.1, we present 4-mode MMAs of (1.1), which have spiking and bursting modes, as well as distinct types of $(1^1)^k(1^0)^\ell$ alternator modes. Then, in Section 3.2, we generalize to n-mode MMAs in (1.1), including examples with $n = 5$ and 1^s bursts with different numbers, s, of SAOs. Further, in Section 3.3, we describe how the minimal periods of the MMAs which are time-periodic may be determined.

To construct the general n-mode MMAs, we take advantage of the rich structure of the bursting oscillations of the x-dependent family of ODEs. For the standard parameter set (see Table 1 in Appendix A), the family of x-dependent ODEs (1.3) contains spiking cells, bursting cells, and cells that alternate between 1^0 spikes and 1^1 bursts. Moreover, within the window of alternator modes, there are sub-intervals on which the cells exhibit $(1^1)^k1^0$ MMO attractors, $k = 1, 2, 3, \ldots$. There are also sub-intervals on which the cells exhibit $1^1(1^0)^\ell$ MMO attractors, $\ell = 1, 2, 3, \ldots$. The single-cell ODE model also possesses parameter regions in which the attractors of the x-dependent family of ODEs exhibit 1^s bursts with various s, which we use in Section 3.2.

3.1 Four-mode MMAs with different types of alternator modes

The first example of a 4-mode MMA is obtained with a Gaussian applied current for $\alpha = 4, \beta = 90$ and $p = 0.4$ (see Appendix A), and these correspond to $I_{\text{base}} \approx 0.0482$ mA, $I_{\max} \approx 0.9033$ mA, and $\sigma \approx 71.03$ in (1.2). All other parameters fixed at their usual values as in the base case studied in Section 2. The MMA exhibits four different modes of activity, and is period-3 (Fig. 6). In the bursting region ($0 \le x \lesssim 10$), the MMA is in the 1^1 bursting mode. Here, the three branches of the (blue) APD consist of diamonds and essentially lie on top of each other, since each has one SAO and they are close to being identical. In the interval $15 \lesssim x \lesssim 24$, the MMA exhibits a $(1^1)^21^0$ alternator mode ($k = 2$) in which one period consists of two 1^1 bursts followed by a 1^0 spike. In this first alternator region, there are three distinct branches of the APD, with the top two branches (blue diamonds) denoting the bursting oscillations and the bottom branch (blue circles) being the spiking oscillation. This pattern repeats, so that this mode of the attractor has period 3. In the interval $24 \lesssim x \lesssim 27$, the MMA exhibits a $1^1(1^0)^2$ alternator mode also of period 3. In this second alternator region, the APD has one branch of burst events (blue diamonds) and two lower branches of spiking events (blue circles). Finally, in the spiking region ($27 \lesssim x \le 50$), the MMA is in the 1^0 spiking mode, and the APD consists exclusively of three branches of blue circles in this spiking region. Overall, this four-mode MMA has 3 events per period, which is the least common multiple of the periods of the component rhythms.

Each of the blue APD branches contains an inflection point along the segment on which it is monotonically decreasing, indicating the presence of maximal spatio-temporal canards in the transition intervals between modes with different numbers of small oscillations. Specifically, in the transition interval ($10 \lesssim x \lesssim 15$) between bursting and $(1^1)^21^0$ alternation, there is an inflection point (at $x \approx 15$) in the lowermost APD profile corresponding to the loss of a small oscillation in every third event. There are inflection points at $x \approx 25$ and $x \approx 27$. These correspond, in order of increasing x, to the loss of a small oscillation in the transition from the $(1^1)^21^0$ alternator mode to the $1^1(1^0)^2$ alternator mode, and to the loss of a small oscillation in the transition from the $1^1(1^0)^2$ mode to the spiking mode.

The n^{th} full return maps, $\left(\Pi_x^S \circ \Pi_x^A\right)^n$, were also calculated for the MMA for $n = 1, 2, 3$. The 3^{rd} full return time (not shown) is the first of these which is constant in x, which confirms that the MMA is period-3.

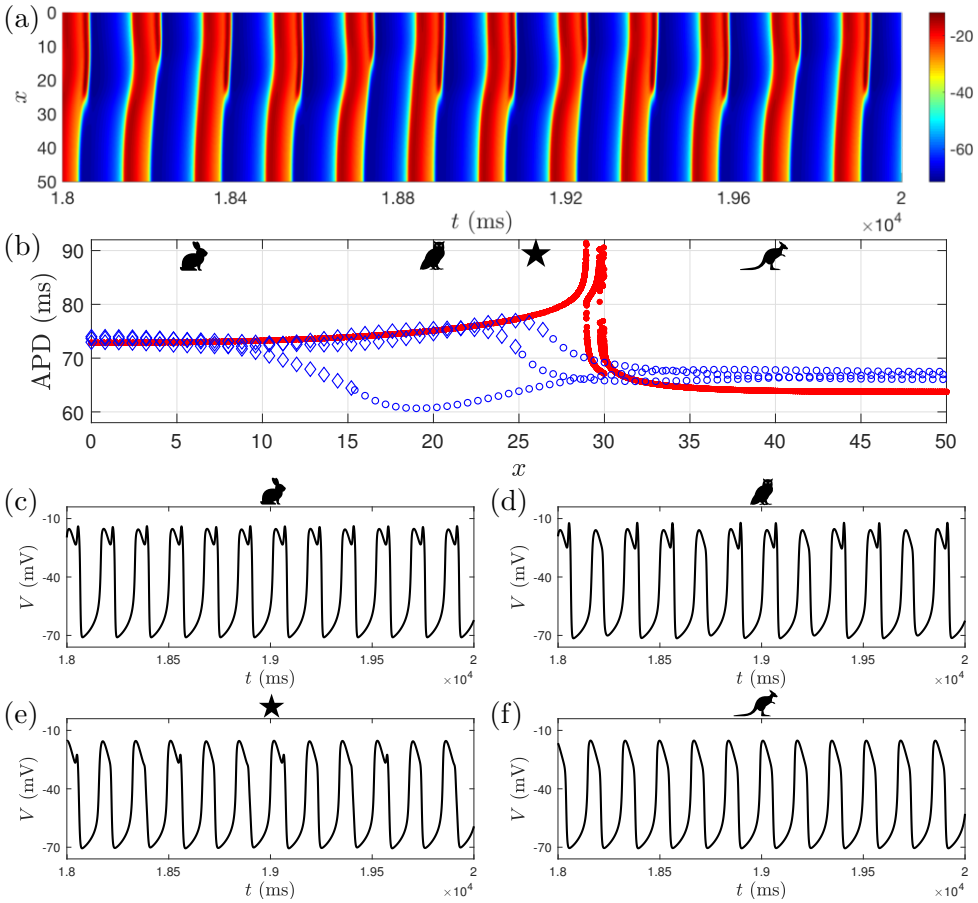

Figure 6: Dynamics of a 4-mode MMA (of period 3) of (1.1) with $\alpha = 4, \beta = 90$, and $p = 0.4$, corresponding to $I_{\text{base}} \approx 0.0482$ mA, $I_{\max} \approx 0.9033$ mA, and $\sigma \approx 71.03$ in (1.2), and all other parameters set at the standard values. (See Section 4 for the relation between the control parameters α, β, p and $I_{\text{base}}, I_{\max}, \sigma$.) (a) Voltage dynamics of the MMA. (b) The APD profiles of the MMA (blue curves) show that it has 4 distinct modes of activity; burst/spike events are indicated by open diamonds/circles. For $0 \le x \lesssim 15$, the attractor is in the 1^1 bursting mode. A representative time series (for $x = 6$; rabbit marker) is shown in (c). For $15 \lesssim x \lesssim 25$, the attractor is in the $(1^1)^2 1^0$ alternator mode. A representative time series (for $x = 20$; owl marker) is shown in (d). For $25 \lesssim x \lesssim 27$, the attractor is in the $1^1(1^0)^2$ alternator mode. A representative time series (for $x = 26$; star marker) is shown in (e). For $27 \lesssim x \le 50$, the MMA is in the 1^0 spiking mode. A representative time series (for $x = 40$; kangaroo marker) is shown in (f). The APD profiles of the family of x-dependent ODEs (red curves) are also shown for comparison.

Another example of a 4-mode MMA is shown in Fig. 7 for $\alpha = 10, \beta = 4$, and $p = 0.4$, corresponding to $I_{\text{base}} \approx -0.0058$ mA, $I_{\max} \approx 0.1292$ mA, and $\sigma \approx 554.92$ in (1.2). This second 4-mode MMA consists of a bursting region ($0 \le x \lesssim 17.5$) in which the attractor is also in the 1^1 bursting mode, just as in the above example. However, for this 4-mode MMA, the cells in the bursting region oscillate with minimal period four (not period one), since the APD has four distinct branches (blue diamonds) and the SAOs have different heights and durations in each of the four events per period (see Fig. 7(b) and (c)). Next, there is a $(1^1)^3 1^0$ region ($17.5 \lesssim x \lesssim 29$) in which the attractor is in this $k = 3$ alternator mode. The APD has three branches of bursting oscillations (blue diamonds), each with SAOs of distinct heights and durations, and one branch of spiking (blue circles). This is followed by a second alternator region ($29 \lesssim x \lesssim 32.5$) in which the attractor is in the $(1^1)^2(1^0)^2$ mode ($k = 2, \ell = 2$), and the APD has two (upper) branches of burst events and two

(lower) branches of spike events per period. Finally, there is a region of $1^1(1^0)^3$ alternator modes ($32.5 \lesssim x \lesssim 50$) in this 4-mode MMA, and the APD has three branches of spiking events and only one branch of burst events per period.

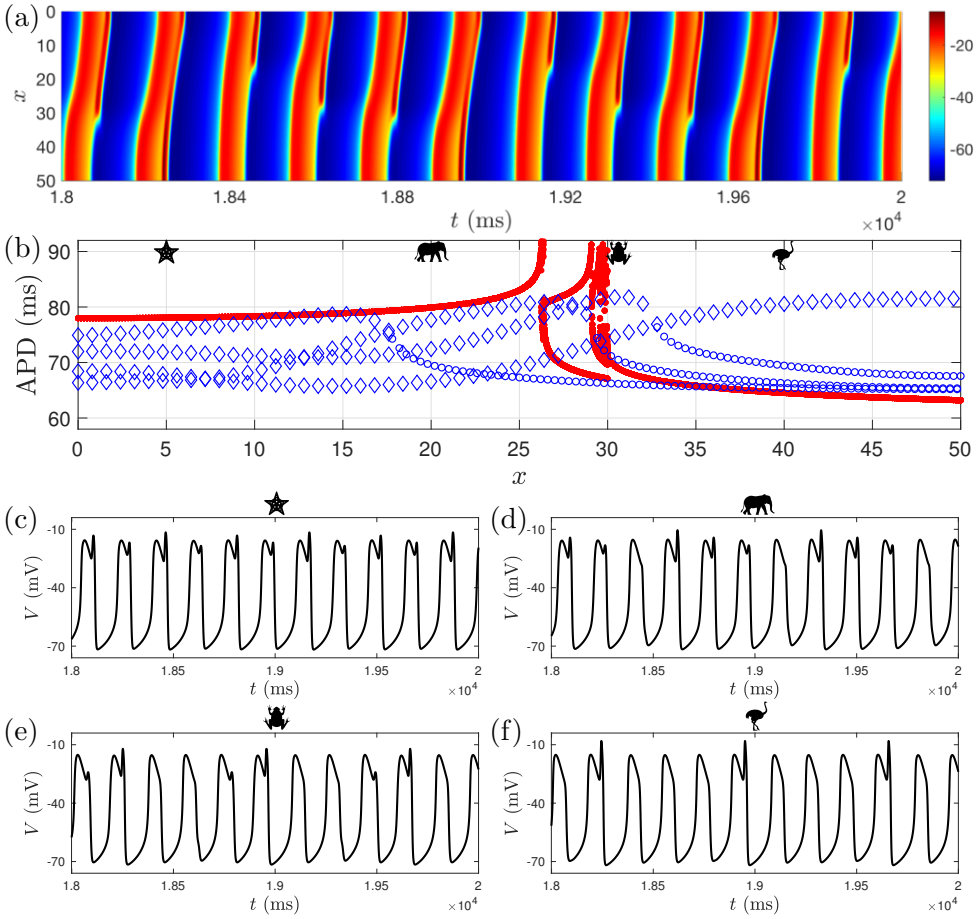

Figure 7: Dynamics of a 4-mode MMA (of period 4) of (1.1) with $\alpha = 10, \beta = 4$ and $p = 0.4$, corresponding to $I_{\text{base}} \approx -0.0058$ mA, $I_{\max} \approx 0.1292$ mA, and $\sigma \approx 554.92$ in (1.2), with all other parameters fixed at their standard values. (See Section 4 for the relation between α, β, p and $I_{\text{base}}, I_{\max}, \sigma$.) (a) Voltage dynamics of the MMA. (b) APD profiles (blue curves) with burst/spike events indicated by diamonds/circles. The all-diamond branch corresponds to the 2^{nd}, 6^{th}, and 10^{th} active bursting red bands in (a). The other three branches possess inflection points where the SAO of the burst disappears. Representative time series from each of the four regions are shown. Starfish: 1^1 bursting. Elephant: $(1^1)^3 1^0$. Frog: $(1^1)^2(1^0)^2$. Ostrich: $1^1(1^0)^3$.

We conclude this subsection with three observations. First, the 4-mode MMA in Fig. 7 has period 4, in contrast to the 4-mode MMA of period-3 shown in Fig. 6. This is because each of the four distinct modes is of period 4. Second, along the monotonicaly decreasing segments of the APD branches of the 4-mode MMA shown in Fig. 7, there are inflection points (marked by the switches from diamonds to circles) that correspond to the transition points in space where small oscillations are lost. Third, the fact that this 4-mode MMA is more complex is expected, based on the known dynamics of the family of x-dependent ODEs (Fig. 7(b), red).

3.2 n-mode MMAs with different types of 1^s bursts

So far, we have studied MMAs of (1.1) with 3 and 4 modes, which possess 1^0 spiking, 1^1 bursting, and $(1^0)^k(1^1)^\ell$ alternator regions. We now consider n-mode MMAs that emerge in (1.1) when the applied current is such that the set of attractors of the x-dependent ODEs (1.3) consists of 1^s pseudo-plateau bursts for $s = 1$ up to $s = N$, for general N.

A representative example of a 5-mode time periodic MMA of (1.1) is shown in Fig. 8. For each fixed x, the temporal profile of the solution is a 1^s pseudo-plateau burst, where $s \in \{2, 3, 4, 5, 6\}$. Cells near the left edge of the domain (i.e., near $x = 0$) exhibit bursts with 6 SAOs. As x is increased towards the right edge (i.e., towards $x = L$), the number and amplitudes of the SAOs continuously change so that $s = 2$ for the cells near the right edge. Thus, the MMA has a region of 1^6 bursts, a region of 1^5 bursts, and so on down to 1^2 bursts.

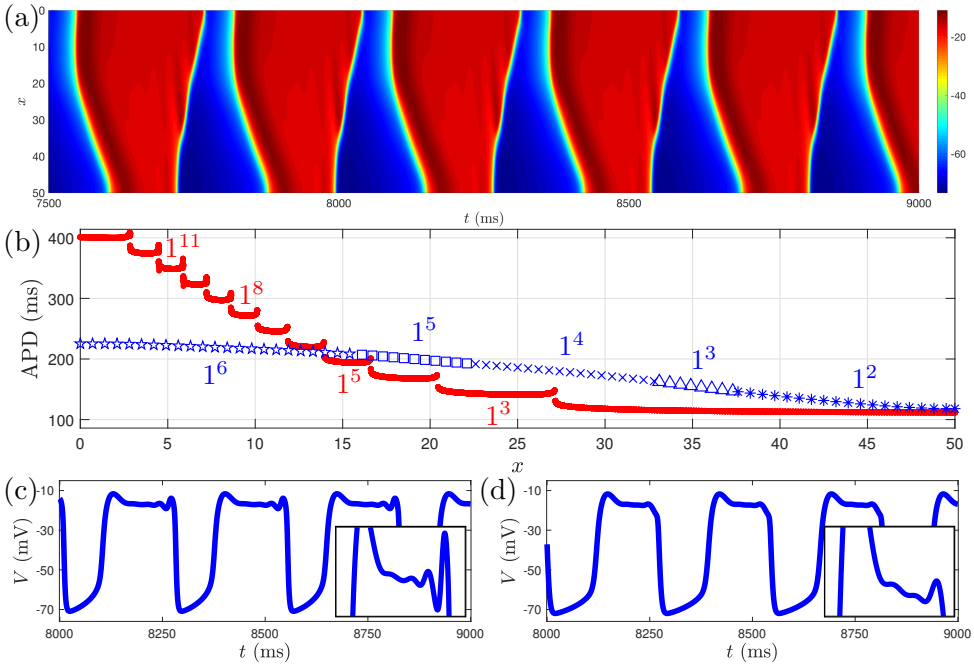

Figure 8: A 5-mode MMA of (1.1) which is time-periodic (with a period of approximately 272 ms). Here, $g_K = 4.4$ nS, and $I_{\text{base}} = -1.5$ mA, $I_{\max} = 5.5$ mA and $\sigma = 150$ in (1.2). (a) The voltage dynamics show that the cells in the region where the applied current has greatest magnitude (near $x = 0$) have the greatest number of small oscillations and hence the longest durations. (b) The APD profile of the 5-mode MMA (blue) compared to the APD measurements of the x-dependent ODEs (red). The number, s, of small oscillations is indicated by the marker type: pentagram for $s = 6$, square for $s = 5$, cross for $s = 4$, triangle for $s = 3$, and asterisk for $s = 2$. Representative time series for the (c) 1^4 bursting mode ($x = 27$) and (d) 1^3 bursting mode ($x = 35$). Insets: zoom on the SAOs.

For this 5-mode MMA, the system parameters are such that the attractors of the family of x-dependent ODEs (1.3) are 1^s pseudo-plateau bursts, where $s = 2, 3, \ldots, 13$ (Fig. 8(b), red curves). Between each pair of 1^{s+1} and 1^s intervals, there exist (extremely thin) alternator regions in which the attractor of (1.3) has Farey sequence $(1^{s+1})^k(1^s)^\ell$, where $k, \ell = 2, 3, \ldots, 13$ (Fig. 8(b), nearly vertical red segments). Despite the fact the x-dependent ODEs span all of the modes from the 1^2 state up to the 1^{13} state, this 5-mode MMA of the PDE only exhibits the 1^2 to 1^6 bursting modes and there are no alternator intervals. This is due to choice of the Gaussian applied current. (With other choices of, for instance, the half-width one can see more distinct modes.) Moreover, in

the transition intervals between the different bursting regions the dynamics of the maximal spatio-temporal canards are slightly different from those observed in the 3-mode and 4-mode MMAs. In particular, some of the SAOs disappear in the merger of two interior SAOs (data not shown). Also, the APD profile of the 5-mode MMA (Fig. 8(b), blue curve) does not show the inflection points that were characteristic of the loss/gain of a small oscillation associated with the transition from a 1^{s+1} region to a 1^s region (cf. blue APD profiles in Figs. 3, 6, and 7). This appears to be due to the fact that, as the amplitude of the last SAO in each event decreases, the amplitude of the SAO immediately preceding it is already increasing.

More generally, an n-mode MMA of (1.1) can easily be constructed. A necessary condition is that the parameter g_K and the control parameters for the Gaussian applied current must be such that the x-dependent ODEs span the 1^s up to 1^{s+N} modes, where $s \geq 0$ and $N \geq 1$. Under these conditions, an n-mode MMA (with $n \leq N$) will generically emerge as an attractor of the PDE (1.1). We have found in our simulations that for N sufficiently large, the inequality $n < N$ is strict and only the 1^s rhythms with smaller s actually manifest in the attractor. The reason why these particular bursting modes (and how many of them) are present in the n-mode MMA is currently unknown and the subject of future work.

3.3 A note about the periods of time-periodic n-mode MMAs

In this brief subsection, we emphasize that —for n-mode MMAs which are periodic in time— the period is determined by the least common multiple of the periods of the modes in the MMA. This was already observed for 4-mode MMAs in Section 3.1, where we presented one with period 3 (recall Fig. 6) and one with period 4 (recall Fig. 7). For the former, each of the spiking, bursting, and two different alternator modes are of period 3. For the latter, each mode is period 4.

In order to show more generally that this is how the periods of n-mode MMAs are determined, we return to 3-mode MMAs. The base case 3-mode MMA studied in Section 2 is of period 2, since that is the least common multiple of the periods of the bursting, single alternator, and spiking modes. Here, we present a 3-mode MMA of period 4. For $\alpha = 10, \beta = 6$, and $p = 0.4$, corresponding to $I_{\text{base}} \approx -0.0058$ mA, $I_{\max} \approx 0.1472$ mA, and $\sigma \approx 424.03$ in (1.2), and all other parameters fixed at the base case values, this MMA exhibits three regions of activity and the APD consists of four branches (Fig. 9). For $0 \leq x \lesssim 16$, the attractor exhibits $(1^1)^2(1^0)^2$ alternations with two burst events followed by two spike events in each period. This transitions into a region of $1^1(1^0)^3$ rhythms (for $16 \lesssim x \lesssim 24$) in which each burst is followed by three spikes per period. The cells on $24 \lesssim x \leq 50$ are in the spiking mode. Overall, this 3-mode MMA is period-4, because that is the least common multiple of the individual modes. For confirmation, we also plotted the 4^{th} full return time, $T_4(x)$, and observed it to be constant in x (data not shown). Finally, we note that spatio-temporal canards mediate the loss/gain of SAOs in the transition intervals, as reflected by the inflection points on the two upper APD branches.

4 Robustness of the MMAs

In this section, we analyze the robustness of MMAs under variations in the fundamental parameters of the Gaussian applied current. We focus on the robustness of the base case 3-mode MMA studied in Section 2. Similar observations can be made about the robustness of the 4-mode and n-mode MMAs presented in Sections 3.1 and 3.2.

Recall from (1.2) that a standard representation for Gaussians, centered at the origin, has the

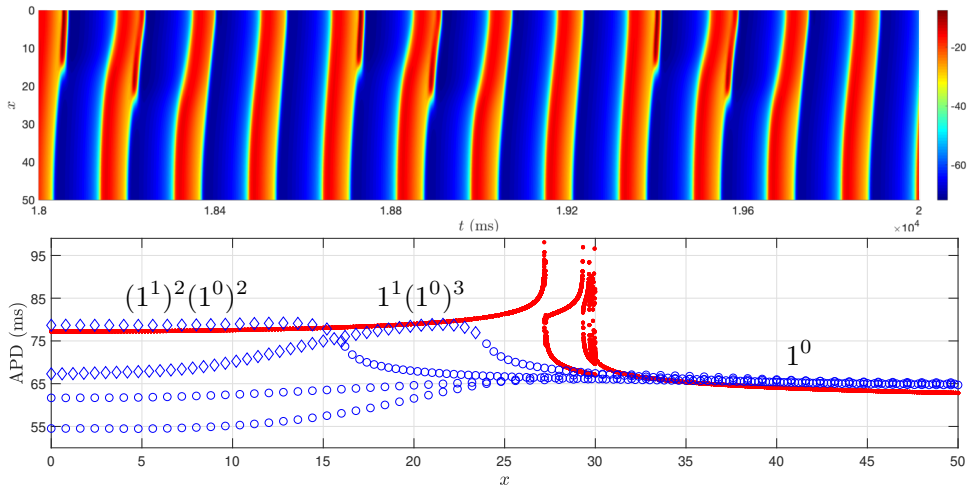

Figure 9: A 3-mode MMA (of period 4) of (1.1) with $\alpha = 10, \beta = 6$ and $p = 0.4$, corresponding to $I_{\text{base}} \approx -0.0058$ mA, $I_{\max} \approx 0.1472$ mA, and $\sigma \approx 424.03$. (We again refer to Section 4 for the relation between α, β, p and $I_{\text{base}}, I_{\max}, \sigma$.) (a) Voltage dynamics over approximately 3 periods. On the interval $0 \leq x \lesssim 16$, the attractor is in the $(1^1)^2(1^0)^2$ alternator mode. On the interval $16 \lesssim x \lesssim 24$, the attractor is in the $1^1(1^0)^3$ alternator mode. For $24 \lesssim x \leq 50$, the MMA is in the spiking mode. (b) The APD profile of the MMA (blue curves) has four branches; open diamonds and circles indicate burst and spike events, respectively. The two uppermost APD branches possess inflection points, corresponding to the boundaries where a SAO vanishes.

form,

$$I_{\text{app}}(x) = I_{\text{base}} + (I_{\max} - I_{\text{base}}) \exp\left(-\frac{x^2}{4\sigma}\right), \tag{4.1}$$

where I_{base} is the baseline applied current, $I_{\max}$ is the maximal applied current, and σ is the half-width of the Gaussian. It turns out to be convenient to measure these three parameters relative to key values of the applied current determined by the family of x-dependent ODEs (1.3), see Fig. 10.

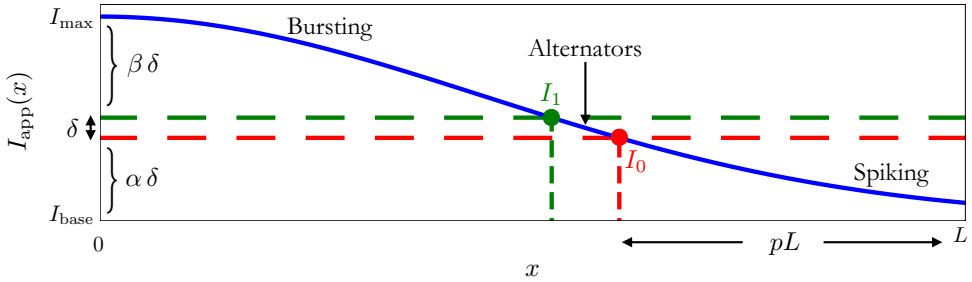

Figure 10: Representative Gaussian applied current, $I_{\text{app}}(x)$, used to generate the base case 3-mode MMA. It partitions the cells of the family of x-dependent ODEs (1.3) into regions of distinct activity. Cells in the bursting region exhibit 1^1 canard-induced mixed-mode oscillations. Cells in the spiking region exhibit 1^0 relaxation oscillations. Cells in the alternator region can exhibit simple $1^1 1^0$ alternations or have complex signatures of the form $(1^1)^k(1^0)^\ell$, especially for x such that $I_{\text{app}}(x) \approx I_0$ or $I_{\text{app}}(x) \approx I_1$. (For the other MMAs reported on, the Gaussian applied current is chosen to cross other bifurcations of the x-dependent ODEs including $I_2, I_3, \ldots$.)

In particular, let I_0 be such that for each x for which $I_{\text{app}}(x) < I_0$ the x-dependent ODE (1.3) is in the 1^0 spiking mode. Similarly, let I_1 be such that for each x for which $I_{\text{app}}(x) > I_1$ the x-dependent ODE (1.3) is in the 1^1 bursting mode. Also, let $\delta = I_1 - I_0$. This parameter δ measures

exactly the width of the interval (I_0, I_1) over which the family of x-dependent ODEs (1.3) exhibits alternating states.

Then, we set

$$I_{\text{base}} = I_0 - \alpha\,\delta, \qquad \text{and} \qquad I_{\max} = I_1 + \beta\,\delta.$$

Here, α and β measure how deeply the applied current brings the cells into parameter regimes corresponding to the spiking and bursting modes of (1.3), respectively. Also, let p denote the percentage of the cells in the line of cells which are in the spiking mode, i.e., let p be such that the cells with $x \in [L - pL, L]$ exhibit 1^0 spiking, based on (1.3); see Fig. 10.

Remark. *The half-width of the Gaussian is related to the three parameters p, α, and β via*

$$\sigma = \frac{1}{\log\left(1 + \frac{1+\beta}{\alpha}\right)} \left[\frac{L}{2}\,(1-p)\right]^2. \tag{4.2}$$

Variations in each of these three control parameters, p, α, and β, offer a natural way to measure how the fundamental properties of the Gaussian impact the robustness of the base case 3-mode MMA. Considering each of these control parameters separately, we plot in Fig. 11 the modes of the attractor of the PDE (1.1) as functions of these control parameters and of the location $x \in [0, L]$. The other system parameters in (1.1) are kept fixed at the same values as in Section 2. The spatial regions in which the MMA is in the 1^1 bursting mode, the $1^1 1^0$ alternator mode, and the 1^0 spiking mode are indicated in blue, green, and red, respectively. We examine the results in each of the frames in Fig. 11, beginning with frame (a), which shows the robustness of the 3-mode MMA to variations in p.

All three modes of the MMA persist across the entire range of p values shown in Fig. 11(a), where we note that the values of α and β used to generate the data shown in Fig. 11(a) are the same as those in the base case in Section 2. Moreover, for each fixed p, the spiking region occupies approximately the same fraction of the spatial domain as predicted from the family of x-dependent ODEs (1.3). For example, for $p = 0.4$, the spiking region observed in the PDE (1.1) is approximately $26 \lesssim x \leq 50$, which is 48% of the domain, and this is close to the interval $30 \leq x \leq 50$ over which the family of x-dependent ODEs (1.3) is in the spiking mode. Similarly, for $p = 0.6$, the spiking region observed in the PDE (1.1) is $18 \lesssim x \leq 50$, which is 64% of the domain, and this is close to the interval $20 \leq x \leq 50$ over which the family of x-dependent ODEs (1.3) is in the spiking mode. These two examples are representative, in that the spiking region in the PDE (1.1) is close to the interval observed in (1.3) for all other values of p in the range simulated. The difference in measurements between the PDE (1.1) and the family of x-dependent ODEs is due to the spatial coupling and will be discussed further in Section 6.

Not only does the width of the spiking region increase with increasing p, as shown in Fig. 11(a), but also the location of the alternator region shifts, and the widths of the alternator and bursting regions decrease. The decreased width of the alternator region may be understood as follows. Recall from (4.2) that increases in p are equivalent to (quadratic) decreases in the spread, σ, so that the Gaussian becomes narrower. Consequently, the x locations at which $I_{\text{app}}(x) = I_0$ (where the 1^0 spikes change stability) and $I_{\text{app}}(x) = I_1$ (where the 1^1 bursts change stability) shift to smaller values, and the slopes of the Gaussian at these locations have increased. Thus, the width of the alternator region decreases.

Next, we study the robustness of the 3-mode MMA under variations in the control parameter α, with p and β kept constant at the same values used in the base case in Section 2; see Fig. 11(b). In this case, the MMA also exhibits the same three regions, and the locations of the transition intervals stay relatively constant, over the range of α shown. That the width of the spiking region

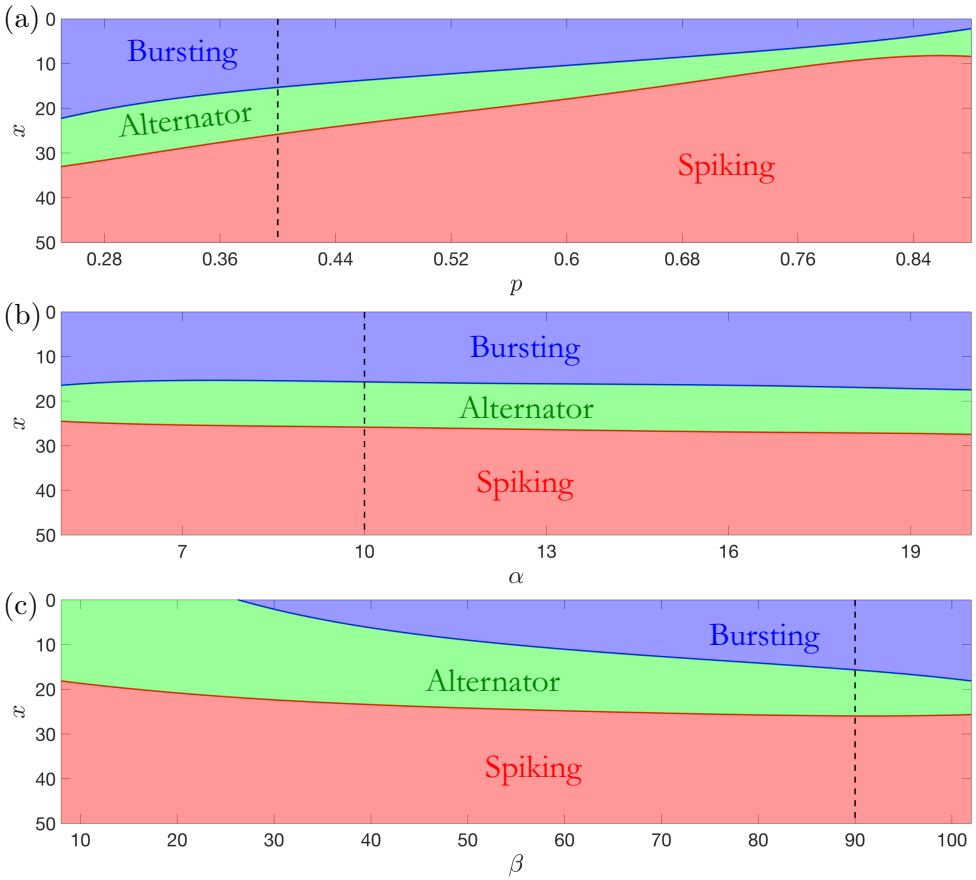

Figure 11: Structure of the MMAs of (1.1) under variations of the control parameters of the Gaussian applied current. The MMAs consist of bursting (blue), $1^1 1^0$ alternator (green), and spiking (red) regions. The base case MMA studied in Section 2 is indicated in each panel by the black dashed line. (a) Increases in the fraction, p, of the cell line that is initialized in the spiking mode results in MMAs with larger spiking regions. (b) Changes in the baseline applied current, via α, have little effect on the widths of the three regions. (c) The maximal applied current, controlled by β, significantly affects the widths of the bursting and alternator regions.

stays nearly constant reflects the fact that p is fixed so that the cells on $30 \leq x \leq 50$ are spiking in (1.3). Moreover, increases in α result in more negative baseline applied currents and only slightly larger spreads, σ. This means the x locations at which the 1^0 and 1^1 modes change stability in (1.3) only vary slightly, which is reflected in the PDE by the nearly horizontal red and blue boundaries. We note that whilst the qualitative trends observed for increasing α can be interpreted in terms of the x-dependent ODE (1.3), the width of the alternator region in the MMA is substantially larger than that predicted by the x-dependent ODE and is a result of the diffusive coupling in (1.1).

Under variations in β, with p and α kept constant at the values of the base case in Section 2, the MMA exhibits either three modes or two modes (Fig. 11(c)). For $\beta \gtrsim 27$, the MMA exhibits three modes: bursting, alternator, and spiking, exactly as in the base case. For these values of β, the width of the bursting region increases with β. This is expected from (1.3) because increases in β make the Gaussian applied current taller and steeper, so the width of the alternator region shrinks. Consequently, a larger portion of the domain (beginning at $x = 0$) for the x-dependent ODEs is in the 1^1 bursting state. In addition, the width of the spiking region saturates (at $x \approx 26$), since p is fixed.

On the other hand, at $\beta \approx 27$, the bursting mode disappears, and for all values of $\beta \lesssim 27$, the MMA only exhibits two modes: spiking and alternator. This is a structural change from the base case 3-mode MMA. Moreover, for $\beta \lesssim 27$, the spiking region occupies a larger domain than is expected from (1.3). For example, for $\beta = 10$ the spiking region occurs on $19 \lesssim x \leq 50$ which is 62% of the domain (whereas only 40% of the domain is spiking in the family of x-dependent ODEs (1.3)). For these values of β, the amplitude of the Gaussian is such that the x-dependent ODE is only weakly in the bursting mode, i.e., β is small enough that many cells in the uncoupled system (1.3) remain close to the bursting/alternator transition interval.

Robustness of the other n-mode MMAs, for $n = 3, 4, 5, \ldots$, may be established in a similar manner. Moreover, in quantitative studies of these MMAs, it is of interest to examine the Gaussian applied current with control parameters I_{base}, $I_{\max}$, and σ based on the values of I_s, for $s = 0, 1, 2, \ldots$, which are known from the ODE kinetics as the boundaries in parameter space for the 1^s bursts.

5 Comparison With the ODE Critical and Slow Manifolds

In this section, we make a qualitative comparison of the structures of the base case 3-mode MMA of the PDE (1.1) for $D = 1$ with the geometric structures that organize the family of x-dependent ODEs, i.e., the critical and slow invariant manifolds of (1.3). We show that the attractor of the PDE stays close to the geometric structures of the family of x-dependent ODEs for large diffusivities by comparing the MMA to the critical and slow manifolds of the underlying ODEs at fixed slices in x (Fig. 12).

5.1 Geometric structures of the family of x-dependent ODEs

We begin with the geometric structures of the x-dependent family of ODEs (1.3) that exist in the singular limit (i.e., for $\varepsilon \propto C_m \to 0$) for the base case parameter set. For each fixed x, the slow/fast system (1.3) possesses a cubic-shaped critical manifold, $S^0(x)$, which has outer attracting sheets, $S^0_{a,+}(x)$ and $S^0_{a,-}(x)$, and an inner repelling sheet, $S^0_r(x)$ (Fig. 12; left column, blue surface). These are separated by curves, $L_+(x)$ and $L_-(x)$, of fold bifurcations of the layer problem (Fig. 12; left column, red curves). That is, the critical manifold is partitioned as

$$S^0(x) = S^0_{a,+} \cup L_+(x) \cup S^0_r(x) \cup L_-(x) \cup S^0_{a,-}(x).$$

Moreover, there is a folded singularity on $L_+(x)$, which is either a folded node (FN) or a folded focus (FF), depending on the value of x. In the case of the FN, there is an associated singular strong canard (Fig. 12(a); green curve), $\gamma^0_{\text{sc}}(x)$, which (together with $L_+(x)$) encloses the singular funnel region.

Remark. *The curves, $L_+(x)$ and $L_-(x)$, meet in a cusp bifurcation and form a single continuous curve, as shown in Figs. 12(a), (c), and (e). Here, our interest is in the region of phase space centered on the folded singularity, which stays far away from the cusp for the chosen parameter set. That is, $S^0_{a,+}(x)$ from $S^0_{a,-}(x)$ are well separated in the regions of phase space that we examine. (We refer to Figure 8(b) of [41] for more information.)*

Fenichel theory [14, 20] and canard theory [36, 43] describe how the geometric objects from the singular limit ($\varepsilon \to 0$) persist and unfold for sufficiently small perturbations (i.e., for $0 < \varepsilon \ll 1$). First, the attracting and repelling sheets, $S^0_{a,\pm}(x)$ and $S^0_r(x)$, of the critical manifold persist as attracting and repelling slow invariant manifolds, $S^\varepsilon_{a,\pm}(x)$ and $S^\varepsilon_r(x)$, respectively. Moreover, in

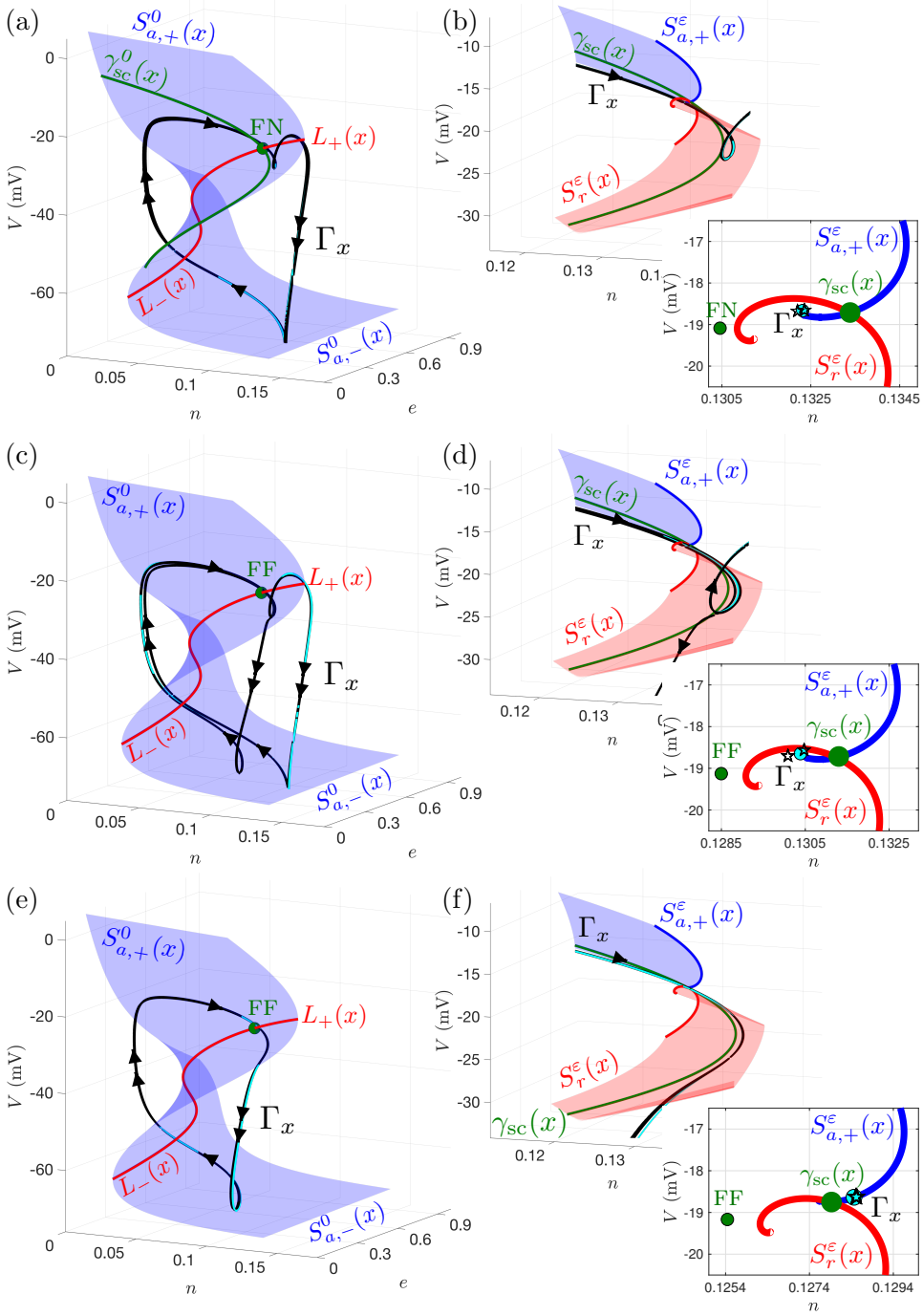

Figure 12: Comparison of the 3-mode MMA (black curves, Γ_x) with the attractor (cyan curves) and manifolds of the x-dependent ODE (1.3) in (V, n, e) space for fixed x in the bursting region (top row; $x = 5$), alternator region (middle row; $x = 17$), and spiking region (bottom row; $x = 40$). Left column: comparison with the singular limit ($C_m \to 0$ pF) structures, i.e., the critical manifold, $S^0(x)$, fold curve, $L(x)$, folded singularity (FN/FF), and singular strong canard, $\gamma^0_{sc}(x)$. Right column: comparison with the attracting (blue surface) and repelling (red surface) slow invariant manifolds of (1.3) for $C_m = 2$ pF, computed using pseudo-arclength continuation [12, 13]. Insets: intersection with a hyperplane through the folded singularity; black pentagrams and cyan circles correspond to the solutions of the PDE and ODE, respectively, and demonstrate that the two are close in each of the three regions.

an $\mathcal{O}(\sqrt{\varepsilon})$ neighbourhood of the FN, $S^{\varepsilon}_{a,+}(x)$ and $S^{\varepsilon}_{r}(x)$ twist around each other and, generically, intersect $n+1$ times, where $n \geq 1$ is determined by the eigenvalues of the desingularized reduced flow at the FN. The first intersection is the primary strong canard, $\gamma_{\rm sc}(x)$, which separates solutions of (1.3) that exhibit SAOs from those that do not. The $n+1^{\rm st}$ intersection is the primary weak canard, $\gamma_{\rm w}(x)$, and is the local axis of rotation for the twisting. Each of the remaining $n-1$ secondary canards (intersections), $\gamma_k(x)$, exhibits k SAOs about $\gamma_{\rm w}(x)$, and separates solutions with k SAOs from solutions with $k+1$ SAOs. For the base case parameters and $x \in [0, L]$, the FNs of (1.3) (whenever they exist) have $n = 1$, so that the only canards are $\gamma_{\rm sc}(x)$ and $\gamma_{\rm w}(x)$, and solutions exhibit, at most, 1 SAO. By varying the parameters g_K and/or g_A, FNs with almost any n can be generated (see Figs. 2, 3, and 5 of [42]).

As the perturbation parameter (in our case, C_m) is increased, the invariant manifolds, the dynamics on the invariant manifolds, and their number of intersections all change. The slow manifolds become less twisted and, for some suitably large C_m, the weak canard of the FN disappears. For $C_m = 2$ pF, the slow manifolds, $S^{\varepsilon}_{a,+}(x)$ and $S^{\varepsilon}_{r}(x)$, intersect precisely once for all $x \in [0, L]$ (Fig. 12; right column). That is, only the strong canard of the FN persists for large perturbations.

The parameter regions where canards exist also change as C_m is increased. For instance, for the parameters used in the base case, the slow invariant manifolds, $S^{\varepsilon}_{a,+}(x)$ and $S^{\varepsilon}_{r}(x)$, of the family of x-dependent ODEs with $C_m = 2$ pF intersect for all $x \in [0, L]$ (Figs. 12(d) and (f)). That is, there is a strong canard for all $x \in [0, L]$, even when the underlying folded singularity of the x-dependent ODE is a FF.

Remark. *We refer to [43] for the bifurcation theory of FN canards when ε is sufficiently small. For a case study on how the slow manifolds and associated family of canards unfold and bifurcate in the unforced pituitary cell ODE model, we point to [42].*

5.2 The MMAs closely follow the slow manifolds in the cores of the main regions

We now compare the geometric structures of the 3-mode MMA of the PDE (1.1) with $D = 1$ to the geometric structure of the family of x-dependent ODEs (1.3). The slow manifolds, maximal strong canard, and solutions of the PDE and ODE are shown in a cross-section passing through the folded node (insets in the right column).

Examining time traces at constant x for each x in the bursting region ($0 \leq x \lesssim 9$), we see that the MMA (Figs. 12(a) and (b), black curves, Γ_x) closely follows the mixed-mode oscillatory attractors (Figs. 12(a) and (b), cyan curve) of (1.3). That is, at each fixed value of x, the time trace of the MMA has a slow segment (lower single arrow) that closely follows $S^0_{a,-}(x)$. The time trace of the MMA passes through the neighbourhood of $L_-(x)$ and exhibits a fast transition (double upward arrows) from a neighbourhood of $S^0_{a,-}(x)$ to a neighbourhood of $S^0_{a,+}(x)$. This fast transition injects the solution into the funnel of the FN. Consequently, at each fixed x in the region, the time trace of the MMA exhibits a slow drift (upper single arrow) toward the FN, where it executes a single SAO before returning to the neighbourhood of $S^0_{a,-}(x)$. For each x in the bursting region, the time trace of the 3-mode MMA (black curve) is so close to the attractor of the corresponding x-dependent ODE (cyan curve) that they are almost indistinguishable.

For all x in the spiking region ($27 \lesssim x \leq 50$), the MMA exhibits relaxation oscillations with slow segments that closely follow the attracting sheets of the critical manifold, and with fast transitions between the upper and lower sheets initiated near the fold curves (Fig. 12(e), Γ_x). In this spiking region, the folded singularity is a folded focus, however, as noted in Section 5.1 the slow manifolds still intersect for large C_m (including $C_m = 2$ pF) in a strong canard (Fig. 12(f), $\gamma_{\rm sc}(x)$). We observe that, for each x in the spiking region, the attractors of the PDE and the x-dependent ODE

stay outside the rotational sector enclosed by $\gamma_{sc}(x)$, and hence there are no SAOs. Again, the solutions of the PDE and ODE lie close to each other in the (V, n, e) phase space.

For x values in the alternator region ($16 \lesssim x \lesssim 22$), the MMA exhibits a 1^1 burst followed by a 1^0 spike. As in the bursting region, the 1^1 part of the solution is a mixed-mode oscillation with the SAO emerging from the canard dynamics around the FN. This 1^1 part of the MMA again lies close to the attractor of the x-dependent ODE (1.3). The 1^0 part of the MMA does not closely follow the attractor of (1.3). However, it does exhibit relaxation-type oscillations, as in the spiking case.

5.3 Only some modes of the x-dependent ODEs emerge in the MMAs, many are suppressed

We now compare and contrast the MMA of the PDE (1.1) and the attractors of the family of x-dependent ODEs (1.3) in the transition intervals between different modes of oscillation, where the maximal spatio-temporal canards arise. We focus on the transition from the bursting mode to the alternator mode, which is representative.

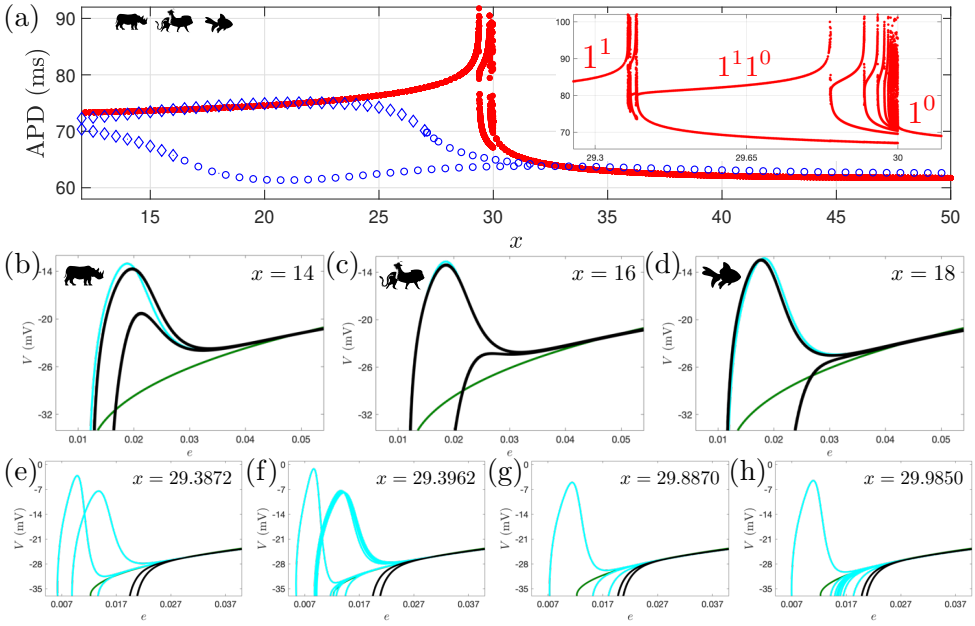

Figure 13: Comparison of the base case 3-mode MMA with the attractors of the family of x-dependent ODEs (1.3) with $C_m = 2$ pF. (a) APD measurements of the MMA (blue branches) and of the ODE attractors (red branches). Inset: zoom on the region featuring alternator modes with complex Farey sequences of the form $(1^1)^k(1^0)^\ell$. Alternators with $k > 1$ (not labelled) exist entirely in the interval between the 1^1 and $1^1 1^0$ branches, and alternators with $k = 1, \ell > 1$ (not labelled) exist entirely in the interval between the $1^1 1^0$ and 1^0 branches. Middle row: projection of the MMA (black), ODE attractor (cyan), and strong canard (green) into the (V, e) plane for x values (b) before, (c) at, and (d) after the first inflection point (at $x \approx 16$) in the APD profile. Bottom row: ODE attractors with (e) $(k, \ell) = (2, 1)$, (f) $(k, \ell) = (5, 4)$, (g) $(k, \ell) = (1, 2)$, and (h) $(k, \ell) = (1, 7)$ for x values in the thin interval between the 1^1 bursting and 1^0 spiking intervals of (1.3). Also shown in all four frames are the strong canard and the trace of the MMA (which is in the spiking mode for $x \gtrsim 27$, i.e., beyond the inflection point of the upper blue APD curve).

The 3-mode MMA, and the attractor and strong canard of the family of x-dependent ODEs are shown in Fig. 13 (middle row) in the (V, e) plane for x values around the inflection point at $x \approx 16$. For all x in this interval, the even burst events (uppermost black curves) in the period-2 MMA closely follow the attractor of the x-dependent ODE (cyan curves). The odd events (lowermost

black curves), however, do not closely follow the ODE attractor. More specifically, to the left of the inflection point, the odd events in the MMA exhibit one SAO in which the orbit has a small upward voltage deflection before rapidly transitioning to a hyperpolarized state (Fig. 13(b)). At successively larger values of x, the SAOs in the odd burst events decrease in magnitude until they disappear at the inflection point at $x \approx 16$ (Fig. 13(c)). For even larger values of x to the right of the inflection point, the odd events in the MMA spend progressively less time following the ODE attractor (i.e., they peel away from the ODE attractor at larger and larger values of e) and simply transition to hyperpolarization without SAOs (Fig. 13(d)). This sequence for the MMA is similar to the sequence of 'jump-back' and 'jump-away' canards (i.e., 'ducks without heads' and 'ducks with heads', respectively) associated with the exponentially close family of canard solutions that can be observed around a maximal canard by variation of initial conditions (see also Figure 13 of [42]). It provides further numerical evidence of the existence of a maximal spatio-temporal canard for some x in the transition interval. A similar jump-back/jump-away canard-like sequence is observed for the MMA in the transition from the alternator region to the spiking region.

The other location where the MMA of the PDE and the attractors of the family of x-dependent ODEs differ significantly from each other is the x-interval where the ODEs exhibit exotic $(1^1)^k(1^0)^\ell$ mixed-mode oscillations. As shown in the inset of Fig. 13(a), the 1^11^0 alternator occupies the largest x-interval. Exotic $(1^1)^k(1^0)^\ell$ alternators with $k \geq 2$ (Figs. 13(e) and (f)) exist entirely in the thin x-interval between the 1^1 bursting branch and the 1^11^0 alternator branch. Similarly, the interval between the 1^11^0 alternator branch and the 1^0 spiking branch is filled with exotic $(1^1)^k(1^0)^\ell$ alternators with $k = 1$ and $\ell \geq 2$ (Figs. 13(g) and (h)).

Numerically, the exotic $(1^1)^k(1^0)^\ell$ alternator modes of the family of x-dependent ODEs are not seen in the MMA of the PDE (for D sufficiently large) because the simpler 1^1, 1^11^0, and 1^0 states exist on wider x-intervals in the domain of the PDE, are more robust and stable, and essentially drive the more exotic alternators out due to the diffusive coupling. The survival of these $(1^1)^k(1^0)^\ell$ alternator modes depends on the parameters (most prominently D and C_m) and the relative widths of the intervals on which they exist in the family of x-dependent ODEs.

In short, in the cores of the main regions of the distinct modes, the MMA of the PDE (1.1) closely follows the geometric structures of the underlying family of x-dependent ODEs, even at large diffusivities. The key similarities and differences highlighted here for the base case 3-mode MMA are representative of n-mode MMAs that exhibit inflection points in their APD profiles, such as those reported on in Sections 3 and 4. The comparison for n-mode MMAs with no inflection points in the APD profiles (such as the 5-mode MMA in Fig. 8) is more complicated, and is the subject of ongoing work.

6 Variations in the Diffusivity

In this section, we show that there is a wide range of diffusivities over which the fundamental structure of the 3-mode MMA stays qualitatively the same as in the base case with $D = 1$. In addition, we show that as the diffusivity becomes smaller and smaller, the dynamics in the alternator region become much more complex.

The APD curves are qualitatively the same as in the base case with $D = 1$ over a broad range of diffusivities (at least $0.01 \leq D \leq 2$) for the 3-mode MMA with these parameters (Fig. 14). For the APD profiles in Fig. 14, the branches are again close to those of x-dependent ODEs in the centres of the three regions. In particular, for all x in the spiking region, the blue and red APD curves are still almost coincident. In addition, for x in the centre of the alternator region, the upper (blue) APD branch (1^1 bursting) stays close to the x-dependent ODE (red) branch, and the lower (blue)

APD branch (1^0 spiking) has shorter durations. Finally, for a large portion (from $0 \leq x \lesssim 8$) of the bursting region, the blue APD branch lies close to the red APD branch.

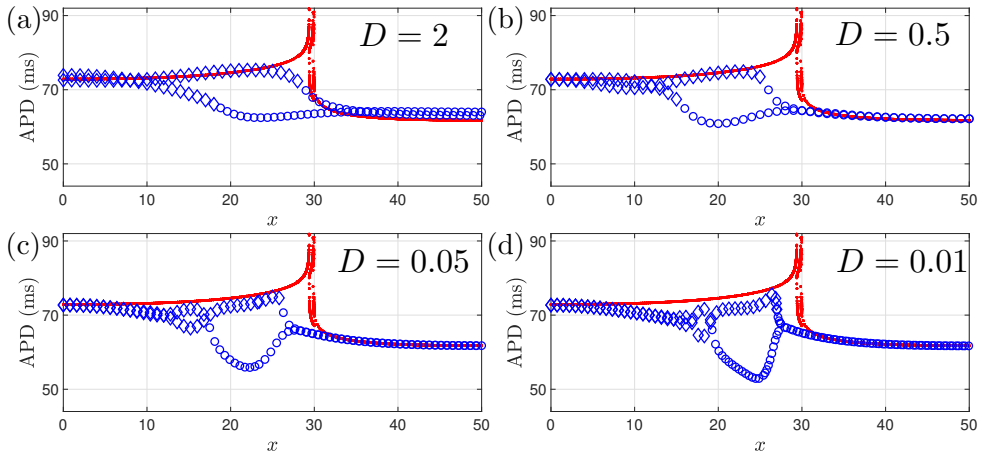

Figure 14: APD profiles of the base case 3-mode MMA (blue curves) for various diffusivities showing two distinct branches. In all panels, an open diamond/circle indicates a burst/spike event. The APD measurements for the family of x-dependent ODEs (red curves) is the same across all panels.

In the transition intervals between the adjacent regions, the APD curves of this 3-mode MMA of the PDE (1.1) also differ here for small values of D from those for the ODE (1.3), as was the case with $D = 1$ in Section 2. In particular, for the locations x in the bursting region close to the transition interval between the bursting and alternator regions, the APD curve splits into two branches which remain close to each other (Figs. 14(a) and (b)). This again reflects the fact that one period of the attractor consists of two burst events, and the durations of the odd and even bursts are slightly different. For smaller D still, the two branches begin to show oscillations in the APD measurements (Figs. 14(c) and (d), near $x \approx 16$).

For smaller diffusivities, D, the spatial structure of the MMAs becomes increasingly complex (the branches of the APD curves cross each other more and more). A representative example, with $D = 0.0005$, is shown in Fig. 15. Here, the voltage dynamics of the MMA (Fig. 15(a)) possess traveling wave structures, which radiate out from a common source at $x \approx 35$. For $0 \leq x \lesssim 35$, the active and silent phases are backward propagating, moving to smaller x values in time. These back-propagating fronts have numerous regions of complex (and seemingly aperiodic) Farey sequences (Fig. 15(b), solid blue curves). For $35 \lesssim x \leq 50$, the activity consists entirely of forward propagating 1^0 spikes (Fig. 15(b), open blue circles).

Based on our simulations, it is currently unknown whether the MMAs of the PDE (1.1) will converge to attractors of the family of x-dependent ODEs (1.3).

7 Bistability

Having introduced and studied an array of n-mode MMAs of (1.1) and demonstrated their robustness in Sections 2-4, as well as having compared them to the various bursting and alternator states of the family of x-dependent ODEs and studied the effects of the diffusivity, D, in Sections 5–6, we now show numerically that the PDE with Gaussian $I_{\text{app}}(x)$ is (at least) bistable. Over a large regime of parameter space, there also exists a time-periodic single-mode attractor, which consists entirely of 1^1 bursting (Fig. 16). It is periodic because the first full return times of the composite map $\Pi_x^S \circ \Pi_x^A$ are uniform in x (not shown). Most interestingly, the amplitudes of the SAOs in the

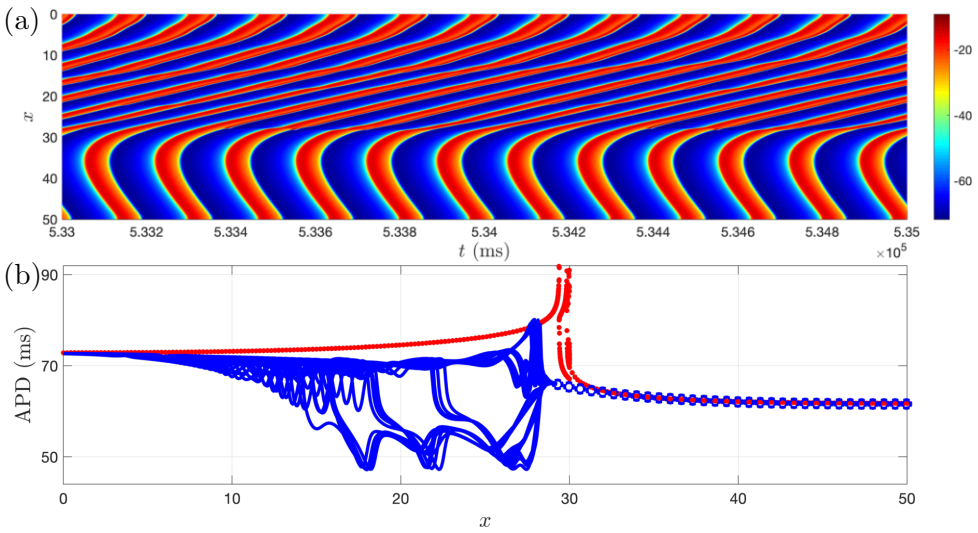

Figure 15: The structure of the MMA becomes increasingly complex in the limit as $D \to 0$. Here, $D = 0.0005$. (a) The voltage dynamics consist of backward propagating waves of $(1^1)^k(1^0)^\ell$ activity and forward propagating waves of 1^0 spiking activity. (b) The APD measurements for 20 successive events in the MMA show the complexity of the spatial structure of the attractor.

single-mode attractor vary with position (Figs. 16(b), (c) and (d)).

For a wide range of initial conditions, all solutions were observed to converge to one of two attractors: the base case MMA with three regions (Fig. 2) or the single-mode bursting attractor (Fig. 16). We verified this by performing 100 simulations of (1.1) subject to (A.2) with the randomized initial conditions, $u_0(x) = (-75 + 95X(x), X(x), X(x))$, where, for each fixed x, $X(x) \sim U(0,1)$ is a uniformly distributed continuous random variable on the unit interval. Moreover, we observed the same type of bistability for all p, α, and β shown in Fig. 11.

The presence and persistence of the single-mode bursting attractor is not predicted by the family of x-dependent ODEs (1.3). In fact, the attractors of the family of x-dependent ODEs are identical for the single-mode bursting attractor and for the base case 3-mode MMA; compare Figs. 3(c) and 16(b), which have the same (red) APD profiles for the x-dependent ODEs but different (blue) APD profiles for the attractor of the PDE.

8 Spatial Inhomogeneity Facilitates MMAs

Until this point, we have focused exclusively on the MMAs of the PDE (1.1) generated by Gaussian applied currents (1.2), which model localized currents. In this section, we show numerically that MMAs are also observed for several other types of applied current profiles, which reinforces the notion that spatial heterogeneity is a key factor that facilitates the emergence of MMAs in (1.1).

First, we study mollified (decreasing) step currents of the form

$$I_{\text{app}}(x) = I_{\text{base}} + \frac{I_{\text{max}} - I_{\text{base}}}{2}\left(1 + \tanh\left(\frac{x_0 - x}{\rho}\right)\right). \tag{8.1}$$

Under variations of the control parameters I_{base} and I_{max} (which are distinct from those of the Gaussian), the PDE exhibits all of the behaviours reported previously, including the n-mode MMAs, maximal spatio-temporal canards mediating the transitions, robustness with respect to parameter changes, as well as bistability with single-mode bursting attractors. For representative illustrations,

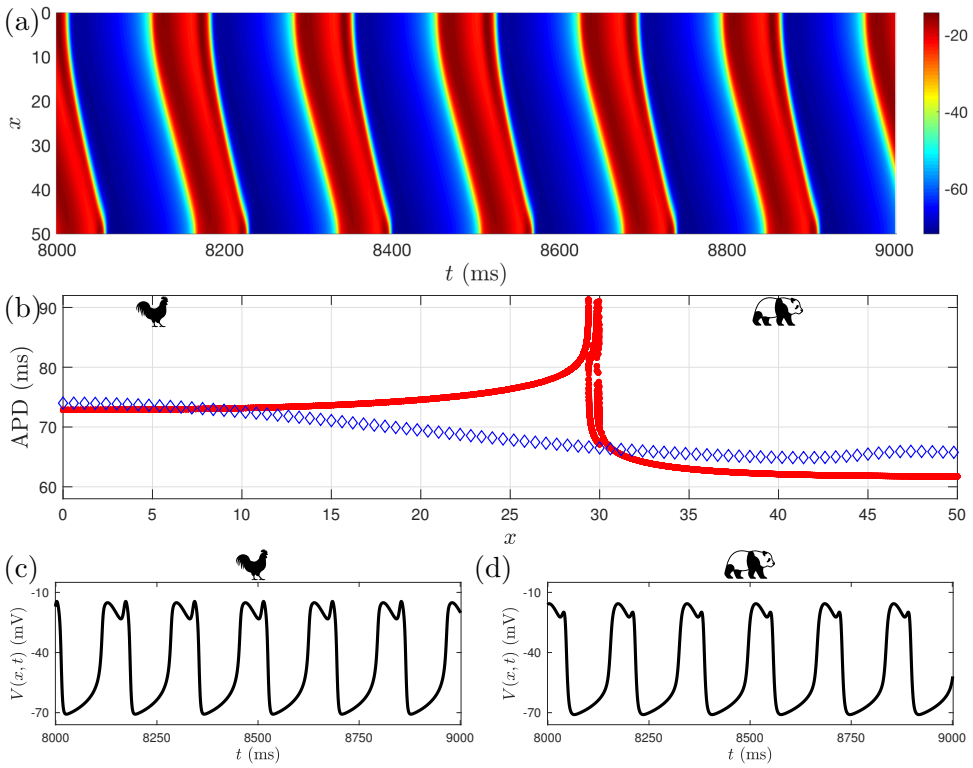

Figure 16: Single-mode time periodic 1^1 bursting attractor (with period approximately 170 ms) of (1.1) with the same parameter set as in Figs. 2 and 3. (a) The voltage dynamics show that the SAOs (dark wine red segments) persist for all x. (b) APD profiles of the single-mode attractor (blue diamonds) and the x-dependent ODE (red), cf. panel (c) of Fig. 3. (c) Voltage series at $x = 5$. (d) Voltage series at $x = 40$.

we show 3-mode and 5-mode MMAs (see Fig. 17). These and other n-mode MMAs are produced by constructing the applied current (8.1) based on the knowledge of the attractors of the x-dependent ODEs (1.3), just as was done in the case of the Gaussian applied current in Sections 2 and 3.

Second, MMAs are also observed for other applied current profiles $I_{\text{app}}(x)$, including sigmoids and mollified bumps, as well as for spatially varying conductances, $g_K(x)$ and $g_A(x)$. To understand the PDE dynamics in these cases, it is also useful to compare to the known dynamics of the single-cell ODE model, for which the boundaries in parameter space of the 1^s bursting and $(1^{s+1})^k(1^s)^\ell$ alternating modes are well known, see Fig. 5 of [42].

9 Discussion

In this section, we summarize our results, present a partial list of open questions, and discuss MMAs in the context of three other reaction-diffusion systems.

9.1 Summary

In this article, we have introduced the novel pattern formation phenomenon of Multi-Mode Attractors observed numerically in a model of pituitary lactotroph cells coupled spatially via diffusion. The n-mode MMAs consist of distinct modes of oscillation in n different regions of the spatial domain. In particular, we have presented 3-mode and 4-mode MMAs in which there are 3, respectively 4, different regions, each exhibiting its own mode of oscillation. The different modes include

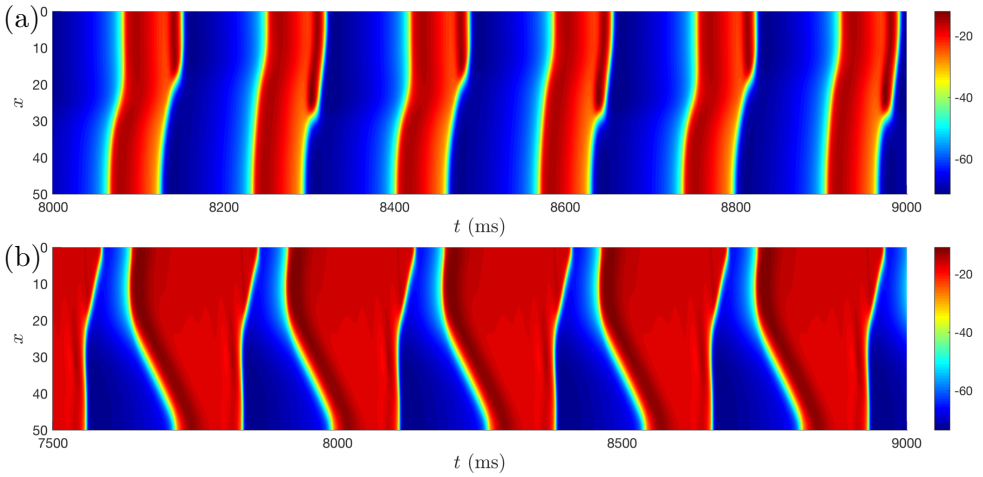

Figure 17: MMAs with (a) 3 modes and (b) 5 modes, obtained by simulating (1.1) with mollified step currents (8.1). (Here, $x_0 = 20$ and $\rho = 10$.) The 3-mode MMA in panel (a) has a 1^1 bursting region ($0 \leq x \lesssim 19$), a $1^0 1^1$ alternator region ($20 \lesssim x \lesssim 27$), and a 1^0 spiking region ($28 \lesssim x \leq 50$). The same parameters were used as in Fig. 2, i.e., $g_K = 6.1$ nS, $\alpha = 10$ and $\beta = 90$, so that $I_{\rm base} \approx -0.0058$ mA and $I_{\rm max} \approx 0.9033$ mA in (8.1). For the 5-mode MMA in panel (b), the attractor exhibits 1^s bursting oscillations with s varying with x (with $s = 6$ near $x = 0$ and $s = 2$ near $x = L$). The same parameters were used as in Fig. 8, i.e., $g_K = 4.4$ nS, $I_{\rm base} = -1.5$ mA, and $I_{\rm max} = 5.5$ mA. The width of the alternator region is larger for larger values of ρ, due to the step from $I_{\rm base}$ to $I_{\rm max}$ being more gradual for larger ρ.

1^0 spiking, 1^1 bursting (with one SAO at the end of the active phase), as well as various types of $(1^1)^k(1^0)^\ell$ alternators, with $k, \ell = 1, 2, \ldots$. We have also presented the existence of 3-, 4-, 5-, and n-mode MMAs in which the modes consist of 1^s bursts with $s = 1, 2, 3, \ldots$ small-amplitude oscillations, with s increasing from one region to the next.

The n distinct regions in n-mode MMAs are generated by applied currents that vary spatially. We have extensively studied Gaussian applied currents as a model for spatially-localized currents, for which the maximum amplitude is at one end of the line of cells and the amplitude decreases in space. We have also studied mollified step function applied currents, in which half of the cells receive one level of constant current and the other half a different level of constant current. In all cases, it is the spatial variation in the applied current which is responsible for the existence of the n distinct modes of oscillation, and we have used the known mixed-mode oscillatory dynamics of single cells (1.3) and how they vary with applied current to generate the n-mode MMAs.

By carrying out a complete analysis of the base case 3-mode MMAs, we have also discovered that there exist new types of maximal spatio-temporal canards in this (and other) reaction-diffusion models. These maximal spatio-temporal canards lie in the transition intervals between adjacent regions of distinct modes. In particular, by examining how the time traces of the voltage (at constant values of x) change as one varies the location x, we have studied how SAOs are lost in the transition intervals between adjacent regions of 1^1 bursting, $1^1 1^0$ alternation, and 1^0 spiking. In each transition interval, there is a unique value of x such that along the time series at that location the profile of the MMA is a maximal spatio-temporal canard. (Visually, the time trace at this unique location resembles the position of the wool thread in knitting when one pulls it over the tip of the needle!) This is an exciting new type of spatio-temporal canard, complementing those that were found recently in an Amari-type integral differential equation, in which it was shown that the entire solution in space can exhibit a temporal oscillation of canard type [3].

Furthermore, we have shown that the n-mode MMAs with maximal spatio-temporal canards

in the transition intervals are robust, by systematically studying them over broad portions of parameter space. Variations in the fraction p of the cells that are in the 1^0 spiking state, as measured based on the (uncoupled) single cell dynamics (1.3), directly impact in an approximately linear manner the width of the region in which the MMA of the PDE (1.1) is in the spiking mode. Also, increases in the maximum amplitude of the Gaussian applied current directly result in increases in the number of cells (near the location of maximal current) being in the 1^1 bursting mode. Moreover, as the steepness of the Gaussian is decreased, more of the middle region exhibits alternating modes, with the number of $(1^1)^k(1^0)^\ell$ alternator modes with different k and ℓ increasing as the slope becomes less steep in the region between the spiking and bursting regions. This systematic study was carried out explicitly for the base case 3-mode MMA, and (data not shown) the trends are similar for the 4-mode, 5-mode, and higher mode MMAs of this type.

For all aspects of the MMAs summarized so far, the action potential duration (APD) was shown to be a useful diagnostic. At each location x in the domain, the APD measures the length of time for which the voltage is above threshold ($V = -45$ mV in our case). We have shown that the APD curves can be used to identify the types of the modes of oscillation that exist in the different regions, the number of different (and more exotic) types of alternators that exist in n-mode MMAs, the periods of the oscillations in the distinct regions of the MMA, the period of an overall MMA of the PDE (1.1), as well as the location of the boundary between different modes of the MMA, via inflection points of the APD.

In addition to establishing all of these properties of the MMAs, we have also established the bistability of the model (1.1). In particular, we reported that there is a 1-mode MMA which co-exists with the different types of 3-mode, 4-mode, and 5-mode MMAs, for all of the various parameter regimes reported here. In conjunction with this bistability, we have also analyzed how the form of the initial data influences which attractor is attained. We also found (data not shown) instances in which the reaction-diffusion system (1.1) can exhibit more than two attractors.

Finally, we carried out computational studies of two other important aspects of the geometric structures of the n-mode MMAs. These studies included how the geometric structures of the n-mode MMAs of the PDE (1.1) compare to the geometry of the slow invariant manifolds (and their intersections) which are known from the study of the single pituitary lactotroph cell model (1.3) for each x in the domain, see [42]. For each region in which the MMA exhibits a different mode, we showed that the time traces of the voltage at points x in the domain are very close to the steady states of the corresponding x-dependent ODE over a wide range of x locations in the center of each region. The differences between the two curves from the PDE and the ODE appear near the boundaries of the regions and in the transition intervals between the regions and are caused by the diffusive coupling. Moreover, the intersections of the slow manifolds in the x-dependent ODEs provide a good guide as to the type of the mode that one sees in an MMA at that same location. Furthermore, these computational studies also included an investigation of how the structures of the base case 3-mode MMA change as the diffusivity, D, becomes smaller. We find that the dynamics observed in the base case with $D = 1$ persist over a broad range of diffusivities $(0.01, 2.0)$, at least. Also, we find that the $D \to 0$ limit appears not to be a regular perturbation of the $D = 0$ case (recall Fig. 15), in which the cells at each location x are decoupled, and in which the PDE model reduces to the family (1.3) of uncoupled x-dependent ODEs.

9.2 Open Questions about MMAs in (1.1)

This study raises many questions, which we are currently investigating. First, can one predict more quantitatively how the number of modes and the locations of their different regions depend on the spatial variation of the applied current? For example, for MMAs such as that shown in Fig. 8,

can the number of modes that are observed in the MMA and their locations be determined more quantitatively from the parameters of the applied current? Also, for the base case MMA shown in Fig. 2, can one predict the width of the $1^1 1^0$ alternator region, which is much wider than what is expected based on the family of x-dependent ODEs. More generally, which of the $(1^{s+1})^k (1^s)^\ell$ alternators from the ODE (1.3) persist under diffusive coupling in the PDE (1.1), and how are the widths of the spatial regions in which they appear determined? Second, can one develop a rigorous existence theory for these n-mode MMAs? Third, can one devise a method to determine their stability? and to determine why the system exhibits bistability between the n-mode MMAs and the single-mode 1^1 attractor? Fourth, what can one say about the dynamics of the n-mode MMAs in the limit as $D \to 0$? Fifth, are there infinite-dimensional analogs in the PDE (1.1) of the slow invariant manifolds $S_a(x)$ and $S_r(x)$ that are known to exist in the finite-dimensional phase spaces of each of the x-dependent ODEs with applied current $I_{\rm app}(x)$? If so, what do these manifolds look like? how do they determine the existence and structure of the n-mode MMAs? and do they intersect in maximal spatio-temporal canards? Sixth, beyond the diffusive pituitary cell model (1.1) studied here (and the three models discussed briefly in Section 9.3 below, which also possesses n-mode MMAs), how general is the class of reaction-diffusion models that exhibit n-mode MMAs?

Additional questions arise from the comparison of the MMA results here with some of the many results known for chimera states in coupled oscillators and reaction-diffusion models. First, the results for (1.1) suggest to examine bursting-, spiking-, and alternating modes in the coherent domains of chimera states in coupled oscillators, as well as to examine the boundaries between such coherent domains and incoherent domains, among other things to see if canards can also occur there. Second, as pointed out by an anonymous reviewer, the fact that the MMAs and spatio-temporal canards arise in locally-coupled systems such as (1.1) may provide further impetus to search for chimera states in systems with only local coupling or diffusive coupling.

9.3 MMAs in a Forced van der Pol PDE & in Cardiac Electrical Activity

We have also numerically observed MMAs and the attendant maximal spatio-temporal canards in the spatially-heterogeneous, forced van der Pol PDE system,

$$\begin{aligned} u_t &= v - f(u) + \varepsilon\, D u_{xx}, \\ v_t &= \varepsilon(a(x) - u + b\cos\theta), \\ \theta_t &= \varepsilon\,\omega. \end{aligned} \tag{9.1}$$

Here, $(u, v, \theta) = (u(x,t), v(x,t), \theta(t))$ with $x \in \mathbb{R}$ and $t \geq 0$, $f(u) = \frac{1}{3}u^3 - u$, $b > 0$ is the amplitude of the time-periodic forcing, $\omega > 0$ is the forcing frequency, and the threshold $a(x)$ is spatially heterogeneous. For the case of $D = 0$, in which the PDE reduces to a family of x-dependent ODEs, this model is known to possess folded nodes, folded saddles, and folded saddle-nodes of type I. The various canards generated by these folded singularities in this forced ODE, including the primary strong and weak canards and the secondary canards, have been studied in [7]. Formulas were derived in the (a, b) parameter plane for the curves of primary maximal canards. We used this knowledge of the canards and their bifurcations in the x-dependent ODEs to construct (Gaussian and sigmoidal) functions $a(x)$ that produced different types of n-mode MMAs in the PDE (9.1) for a range of values of the diffusivity D. A representative example is shown in Fig. 18.

Another context in which the MMAs and their associated maximal spatio-temporal canards naturally arise is in cardiac tissue models. In this context, the s small oscillations in the 1^s bursting modes are labelled as early afterdepolarizations, and they are correlated with cardiac arrhythmias. For instance, Liu et al. [26] studied a biophysically detailed 1D cable model (of length L) for the

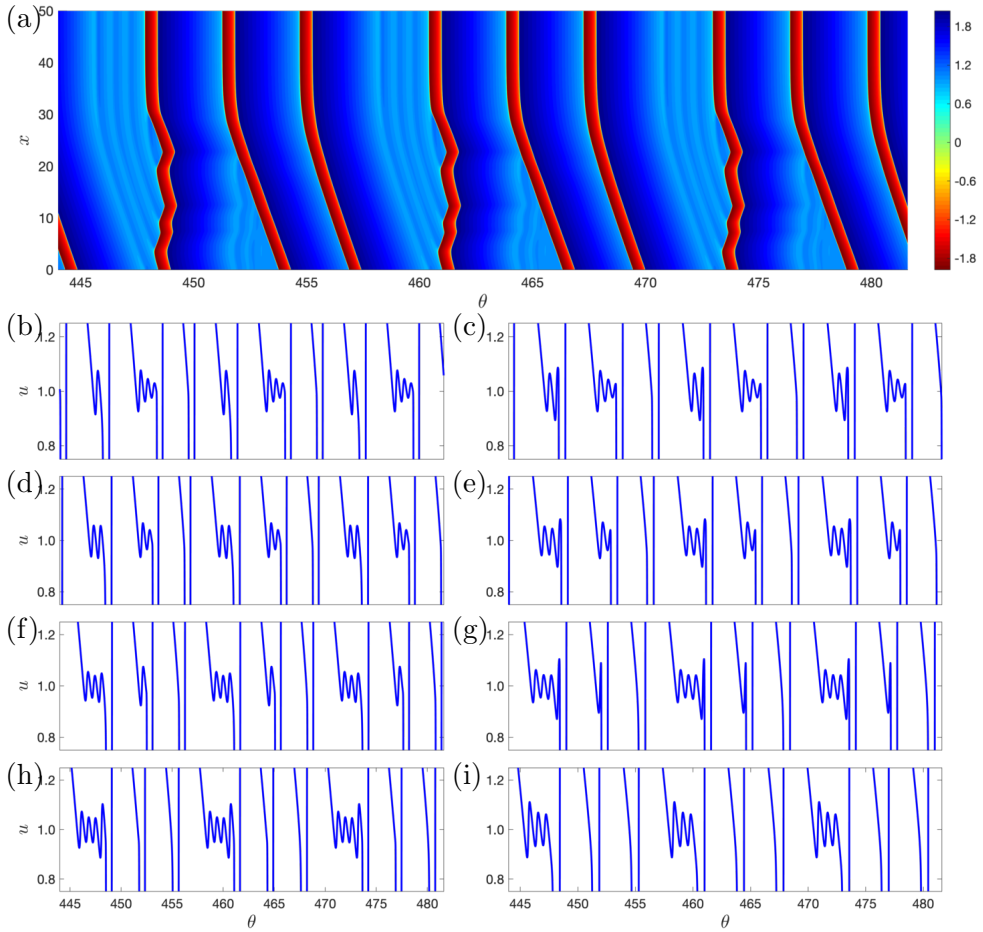

Figure 18: An 8-mode MMA of period-3 of the diffusive forced van der Pol PDE (9.1) for $\varepsilon = 0.01, b = 0.01, D = 1$, and Gaussian threshold $a(x) = 0.9924 + 0.004 \exp\left(-\frac{x^2}{250}\right)$. Each mode is a combination of relaxation oscillations and mixed-mode oscillations of 1^s type for $s = 1, 2, 3$, and 4. (a) Heat map of the u-component of the MMA. (b)–(i) Time series of the different modes, zoomed in on a neighbourhood of $u = 1$ (where folded node canards of the x-dependent family of ODEs are localized). In (b) $x = 3$, (c) $x = 5$, (d) $x = 8$, (e) $x = 10.5$, (f) $x = 15$, (g) $x = 20.5$, (h) $x = 24$, and (i) $x = 35$.

electrical activity in rabbit heart tissue. The model, which consists of 26 (ordinary and partial) differential equations, takes the form

$$C_m \frac{\partial V}{\partial t} = -I_{\text{ion}} + I_{\text{app}}(x,t) + D\nabla^2 V, \tag{9.2}$$

where the ionic currents, I_{ion}, are described using a Hodgkin-Huxley formalism (with associated gating variables), and $I_{\text{app}}(x,t)$ is the stimulus current. Spatial heterogeneity arises from two sources. First, the conductance, g_{Ks}, of the slow component of the delayed rectifier potassium current is a spatial step function,

$$g_{Ks}(x) = \begin{cases} g_{Ks1}, & 0 \le x \le \frac{1}{2}L, \\ g_{Ks2}, & \frac{1}{2}L < x \le L, \end{cases}$$

so that half of the cells in the cable have a maximum I_{Ks} conductance of g_{Ks1} and the other half have a maximum I_{Ks} conductance of g_{Ks2}; this models repolarization and APD heterogeneities.

Second, a stimulus pulse of magnitude 50 μA cm^{-2} and τ ms duration was applied every PCL ms to only 2.5% of the domain

$$I_{\text{app}}(x,t) = \begin{cases} 0, & 0 \le x < \frac{39}{40}L, \\ 50\sum_{k=1}^{\infty}\left[H(t-k\cdot\text{PCL}) - H\left(t-(k\cdot\text{PCL}+\tau)\right)\right], & \frac{39}{40}L \le x \le L, \end{cases}$$

where $H(\cdot)$ denotes the Heaviside function and τ was typically 1 ms. For appropriate choices of the stimulus period (PCL), Liu et al found what appear to be MMAs in the PDE (9.2). In particular, they reported a 2-mode MMA consisting of a $1^1 1^0$ alternator region and a 1^0 region of regular action potentials (see Fig. 2B of [26]). Similarly, they reported two types of 3-mode MMAs; one with a $1^1 1^2$ alternator region, a 1^1 region, and a 1^0 region (see Fig. 2C of [26]) and another with 1^2 region, a 1^1 region, and a $(1^1)^2 1^0$ alternator region (see Fig. 2D of [26]), as well as other MMAs.

We have also observed MMAs in preliminary simulations of a simplified reaction-diffusion model for early afterdepolarizations in cardiomyocytes. The EADs that arise in the kinetics of this simplified model (which consists of only 3 ODEs and is based on [31]) have been demonstrated to be canard-induced [21, 40]. By using our knowledge of these canards in the ODEs, we are able to construct heterogeneities (with the same functional forms as in [26]) such that MMAs exist on large open regions of parameter space in this simplified PDE model for EADs. The MMAs in this system are time periodic as they are entrained to the periodic forcing.

Acknowledgement

The authors thank Arjen Doelman, Ryan Goh, Mark Kramer, Martin Wechselberger, and Arik Yochelis for useful feedback. We are also grateful to the two anonymous referees for their insightful comments and suggestions, which improved the presentation of the results. We also thank the anonymous referee who asked about the possible connection to chimera states. The research of T.V. was supported by Florida State University. The research of R.B. and T.V. was supported by NSF-DMS 1853342. The research of T.K. and T.V. was partially supported by NSF-DMS 1616064. T.V. thanks the University of Sydney for its hospitality during the Soc. Math. Bio. meeting in July 2018, where these results were first presented. T.K. thanks Ben-Gurion University of the Negev for its hospitality during the Advances in Pattern Formation conference in February 2019.

A Pituitary Cell Model

A.1 The Initial-Boundary Value Problem

We consider a line of diffusively-coupled pituitary lactotrophs, based on the model of [39], in which there is nearest neighbour coupling along the line of length L. The model equations are

$$\begin{aligned} C_m\frac{\partial V}{\partial t} &= I_{\text{app}}(x) - (I_{Ca} + I_K + I_A + I_L) + D\frac{\partial^2 V}{\partial x^2}, \\ \frac{\partial n}{\partial t} &= \frac{n_\infty(V) - n}{\tau_n}, \\ \frac{\partial e}{\partial t} &= \frac{e_\infty(V) - e}{\tau_e}, \end{aligned} \tag{A.1}$$

where $V(x,t)$ denotes the membrane potential of the cell at position x along the cell line at time t; $n(x,t)$ denotes the gating variable for the activation of the delayed rectifier potassium current, I_K,

and $e(x,t)$ the gating variable for the inactivation of the A-type potassium current, I_A. The kinetics of (1.1) are based on a minimal model for the electrical activity in a pituitary lactotroph [39]. The intrinsic ionic current, I_{ion}, consists of calcium, delayed-rectifier potassium, A-type potassium and leak currents, which are defined via Ohm's law by

$$\begin{aligned} I_{Ca} &= g_{Ca} m_\infty(V)(V - V_{Ca}), \\ I_K &= g_K n(V - V_K), \\ I_A &= g_A a_\infty(V) e(V - V_K), \\ I_L &= g_L(V - V_K). \end{aligned}$$

The steady state activation and inactivation functions are sigmoids of the form

$$u_\infty(V) = \frac{1}{1 + \exp\left(\frac{V_u - V}{s_u}\right)},\ u \in \{m, n, a\} \quad \text{and} \quad e_\infty(V) = \frac{1}{1 + \exp\left(\frac{V - V_e}{s_e}\right)}.$$

The applied current, $I_{\text{app}}(x)$, is spatially dependent. Our choice of standard parameter set is taken from [42] and is listed in Table 1. With this choice of parameters, and in the absence of diffusion and with $I_{\text{app}}(x) \equiv 0$, each cell is a 1^0 spiking cell.

Param	Value	Param	Value	Param	Value	Param	Value
C_m	2 pF	g_K	6.1 nS	g_A	5 nS	g_{Ca}	2 nS
g_L	0.3 nS	V_{Ca}	50 mV	V_K	-75 mV	V_m	-20 mV
V_n	-5 mV	V_a	-20 mV	V_e	-60 mV	s_m	12 mV
s_n	10 mV	s_a	10 mV	s_e	5 mV	τ_n	40 ms
τ_e	20 ms	L	50	D	1 nS		

Table 1: Standard parameters for (1.1); see [42] for their biological interpretation.

For the initial-boundary value problem, we impose zero-flux boundary conditions,

$$V_x(0,t) = 0 \quad \text{and} \quad V_x(L,t) = 0, \tag{A.2}$$

and employ initial profiles of the form

$$u(x,0) = u_0(x), \quad u \in \{V, n, e\}. \tag{A.3}$$

The specific choices are detailed in the main text.

Remark. *The base case 3-mode MMA shown in Fig. 2 was obtained as the time asymptotic solution of* (1.1) *subject to the zero-flux boundary conditions* (A.2) *with the initial condition*

$$u_0(x) = \Gamma_x \cap \{V = -20 \text{ mV}\},$$

where Γ_x *denotes the set of attractors of the family of* x*-dependent ODEs* (1.3)*, with the Gaussian applied current having the same control parameters* I_{base}*,* $I_{\max}$*, and* σ*. More specifically, on* $0 \le x \le 50$ *the initial data was chosen so that the cells with* $30 \le x \le 50$ *are set initially to exhibit spiking oscillations, and the cells for* $0 \le x < 30$ *are set initially to exhibit either alternating or bursting rhythms, according to the steady states of the* x*-dependent ODEs. With this initial data, the transient dynamics reflect these initial rhythms locally. The first band of active phases shows that approximately* 40% *of the domain is in the spiking mode and the remaining* 60% *exhibits a small oscillation before termination of the active phase. As the solution of the PDE evolves in time, the spiking part of the domain appears to invade the bursting part and the two modes occupy approximately equal portions of the spatial domain. Eventually, the solution exhibits the MMA shown in Fig. 2.*

All numerical simulations of the PDE (1.1) subject to the boundary conditions (A.2) with initial conditions (A.3) were performed using balanced symmetric Strang operator splitting [35]. Centered finite differences were used for the Laplacian and boundary conditions, and the time stepping was performed using the fourth-order Runge-Kutta method. The results obtained from centered finite differences were compared with those obtained from spectral methods (with Chebyshev basis functions), and were found to be in excellent agreement in all cases. We also verified our numerical results independently using Crank-Nicolson. Moreover, each simulation was run for at least $8000/\sqrt{D}$ ms to guarantee convergence to the attractor.

A.2 Construction of the Spatially Inhomogeneous Applied Current

To construct n-mode MMAs in the PDE (1.1), it has been especially useful to have detailed knowledge of the bifurcation structure of the family of x-dependent ODEs (1.3), as well as the maximal canards which mediate the bifurcations. Here, for the sake of completeness, we provide a more complete description of the bifurcation structure of the kinetics ODEs.

For the parameter set listed in Table 1 and in the absence of any applied current, the cells in the x-dependent ODE (1.3) are 1^0 spiking cells. The spatial variation in the applied current, $I_{\text{app}}(x)$, can then induce bifurcations. The Gaussian $I_{\text{app}}(x)$ used in Section 2 is constructed so that it crosses two distinct bifurcations of system (1.3) (see Fig. 10). Let I_0 and I_1 denote the applied current values at which the 1^0 spiking orbits and 1^1 bursting orbits change stability, respectively, in the single cell ODE model. Then, in system (1.3), the cells with $I_{\text{app}}(x) > I_1$ exhibit 1^1 pseudo-plateau bursting attractors. Similarly, the cells with $I_{\text{app}}(x) < I_0$ exhibit spiking attractors, and cells with $I_0 < I_{\text{app}}(x) < I_1$ exhibit attractors with alternating signatures that can be simple (e.g., $1^0 1^1$ rhythm) or can be complex. More specifically, cells in the alternator region with $I_{\text{app}}(x) \approx I_0$ exhibit $(1^0)^k 1^1$ attractors for $k \in \mathbb{N}$, whilst cells in the alternator region with $I_{\text{app}}(x) \approx I_1$ exhibit $1^0(1^1)^k$ attractors for $k \in \mathbb{N}$. The stability plateaus of the complex signatures, $(1^0)^k 1^1$ and $1^0(1^1)^k$, are substantially smaller than that of the simple $1^0 1^1$ alternator; see Fig. 2(b) of [42]. That is, in the ODE, the alternator region is dominated by a stable $1^0 1^1$ alternator. Similar statements apply for the 1^s bursting modes and the associated $(1^{s+1})^k (1^s)^\ell$ alternator modes, for $s = 1, 2, \ldots$.

In terms of the slow invariant manifolds and maximal canards, bifurcations of the pseudo-plateau bursting occur in two distinct ways [42]. That bifurcation theory may be applied directly to the family of x-dependent ODEs (1.3). In the first case, parameter variations (such as changes in the maximal conductance of the delayed rectifier potassium channels or the applied current) cause twisting of the attracting and repelling slow manifolds, $S_a(x)$ and $S_r(x)$, of system (1.3). This twisting can lead to a tangency between $S_a(x)$ and $S_r(x)$ that then perturbs to a pair of transverse intersections. In this way, new maximal canards and hence additional small oscillations are generated. In the second case, the structure of the slow manifolds essentially remains fixed with respect to parameter variations (such as changes in the maximal conductance of A-type potassium channels), whereas the position of the pseudo-plateau bursting attractor moves relative to the maximal canards. In this scenario, bifurcations occur when the bursting orbit crosses a maximal canard resulting in the loss or gain of a small oscillation.

References

[1] D. M. Abrams, R. E. Mirollo, S. Strogatz, and D. A. Wiley. Solvable model for chimera states of coupled oscillators. *Physical Review Letters*, 101:084103, 2008.

[2] D. M. Abrams and S. Strogatz. Chimera states for coupled oscillators. *Physical Review Letters*, 93:174102, 2004.

[3] D. Avitabile, M. Desroches, and E. Knobloch. Spatiotemporal canards in neural field equations. *Phys. Rev. E*, 95:042205, 2017.

[4] D. Avitabile, M. Desroches, E. Knobloch, and M. Krupa. Ducks in space: from nonlinear absolute instability to noise-sustained structures in a pattern-forming system. *Proc. R. Soc. A*, 473:20170018, 2017.

[5] X. Bonnefont, A. Lacampagne, A. Sanchez-Hormigo, E. Fino, A. Creff, M. N. Mathieu, S. Smallwood, D. Carmignac, P. Fontanaud, P. Travo, G. Alonso, N. Courtois-Coutry, S. M. Pincus, I. C. Robinson, and P. Mollard. Revealing the large-scale network organization og growth-hormone secreting cells. *Proc. Natl. Acad. Sci. USA*, 102:16880–16885, 2005.

[6] F. Buchholtz, M. Dolnik, and I. R. Epstein. Diffusion-induced instabilities near a canard. *J. Phys. Chem.*, 99:15093–15101, 1995.

[7] J. Burke, M. Desroches, A. Granados, T. J. Kaper, M. Krupa, and T. Vo. From canards of folded singularities to torus canards in a forced van der pol equation. *J. Nonlinear Sci.*, 26:405–451, 2016.

[8] L. Buřič, A. Klíč, and L. Purmová. Canard solutions and traveling waves in the spruce budworm population model. *Appl. Math. Comput.*, 183:1039–1051, 2006.

[9] P. Carter, E. Knobloch, and M. Wechselberger. Transonic canards and stellar wind. *Nonlinearity*, 30:1006–1033, 2017.

[10] P. de Maesschalck, N. Popovic, and T. J. Kaper. Canards and bifurcation delays of spatially homogeneous and inhomogeneous types in reaction-diffusion equations. *Advances in Differential Equations*, 14:943–962, 2009.

[11] M. Desroches, J. Guckenheimer, B. Krauskopf, C. Kuehn, H. M. Osinga, and M. Wechselberger. Mixed-mode oscillations with multiple time scales. *SIAM Rev.*, 54:211–288, 2012.

[12] M. Desroches, B. Krauskopf, and H. M. Osinga. The geometry of slow manifolds near a folded node. *SIAM J. Appl. Dyn. Syst.*, 7:1131–1162, 2008.

[13] M. Desroches, B. Krauskopf, and H. M. Osinga. Numerical continuation of canard orbits in slow–fast dynamical systems. *Nonlinearity*, 23:739–765, 2010.

[14] N. Fenichel. Geometric singular perturbation theory for ordinary differential equations. *Journal of Differential Equations*, 31:53–98, 1979.

[15] P. Gandhi, C. Beaume, and E. Knobloch. Time-periodic forcing of spatially localized structures. In M. Tlidi and M. G. Clerc, editors, *Nonlinear Dynamics: Materials, Theory and Experiments*, volume 173 of *Springer Proceedings in Physics*, pages 303–316, Switzerland, 2016. Springer.

[16] A. Hagerstrom, T. Murphy, R. Roy, P. Hövel, I. Omelchenko, and E. Schöll. Experimental observation of chimeras in coupled-map lattices. *Nature Phys.*, 8:658—661, 2012.

[17] K. Harley, P. van Heijster, R. Marangell, G. J. Pettet, and M. Wechselberger. Existence of traveling wave solutions for a model of tumor invasion. *SIAM J. Appl. Dyn. Syst.*, 13:366–396, 2014.

[18] K. Harley, P. van Heijster, R. Marangell, G. J. Pettet, and M. Wechselberger. Novel solutions for a model of wound healing angiogenesis. *Nonlinearity*, 27:2975–3003, 2014.

[19] J. Härterich. Viscous profiles of traveling waves in scalar balance laws: the canard case. *Methods Appl. Anal.*, 10:97–118, 2003.

[20] C. Jones. Geometric singular perturbation theory. In R. Johnson, editor, *Dynamical Systems, Montecatini Terme*, volume 1609 of *Lecture Notes in Math.*, pages 44–118, Berlin, 1995. Springer.

[21] P. Kuegler, A. E. Erhardt, and M. A. K. Bulelzai. Early afterdepolarizations in cardiac action potentials as mixed mode oscillations due to a folded node singularity. *Plos One*, 13:e0209498, 2018.

[22] C. Kuehn. *Multiple Time Scale Dynamical Systems*, volume 191 of *Applied Mathematical Sciences*. Springer Berlin Heidelberg, 2015.

[23] Y. Kuramoto. Reduction methods applied to nonlocally coupled oscillator systems. In S. Hogan, A. Champneys, B. Krauskopf, M. d. Bernardo, R. Wilson, H. Osinga, and M. Homer, editors, *Nonlinear dynamics and chaos: Where do we go from here?*, pages 209–228. Institute of Physics, Bristol, UK, 2003.

[24] Y. Kuramoto and D. Battogtokh. Coexistence of coherence and incoherence in nonlocally coupled phase oscillators. *Nonlinear Phenomena in Complex Systems*, 5:380–385, 2002.

[25] P. Lakatos, A. Shah, K. Knuth, I. Ulbert, G. Karmos, and C. Schroeder. An oscillatory hierarchy controlling neuronal excitability and stimulus processing in the auditory cortex. *J. Neurophys.*, 94:1904–1911, 2005.

[26] W. Liu, T. Y. Kim, X. Huang, M. B. Liu, G. Koren, B.-R. Choi, and Z. Qu. Mechanisms linking t-wave alternans to spontaneous initiation of ventricular arrhythmias in rabbit models of long qt syndrome. *J. Physiol.*, 596:1341–1355, 2018.

[27] N. N. Nefedov and K. R. Schneider. Delay of exchange of stabilities in singularly perturbed parabolic problems. *Prof. Steklov Inst. Math., (Asymptotic Expansions, Approximation Theory, Topology, suppl. 1)*, suppl. 1:S144–S154, 2003.

[28] E. Ott and T. Antonsen. Low dimensional behavior of large systems of globally coupled oscillators. *Chaos*, 18:037113, 2008.

[29] M. Panaggio and D. Abrams. Chimera states: coexistence of coherence and incoherence in networks of coupled oscillators. *Nonlinearity*, 28:R67, 2015.

[30] J. Rinzel. *A formal classification of bursting mechanisms in excitable systems*, pages 267–281. Lecture Notes in Biomathematics. Springer, Berlin, Heidelberg, 1987.

[31] D. Sato, X. L. Hua, T. P. Nguyen, J. N. Weiss, and Z. Qu. Irregularly appearing early afterdepolarizations incardiac myocytes: Random fluctuations or dynamical chaos? *Biophys. J.*, 99:765–773, 2010.

[32] L. Schmidt, K. Schönleber, K. Krischer, and V. Garcia-Morales. Coexistence of synchrony and incoherence in oscillatory media under nonlinear global coupling. *Chaos*, 24:013102, 2014.

[33] K. R. Schneider, E. A. Shchepakina, and V. A. Sobolev. New type of traveling wave solutions. *Math. Methods Appl. Sci.*, 26:1349–1361, 2003.

[34] S. Shima and Y. Kuramoto. Chimera states: coexistence of coherence and incoherence in networks of coupled oscillators. *Phys. Rev. E*, 69:036213, 2004.

[35] R. Speth, W. Green, S. MacNamara, and G. Strang. Balanced splitting and rebalanced splitting. *SIAM J. Numer. Anal.*, 51:3084–3105, 2013.

[36] P. Szmolyan and M. Wechselberger. Canards in $\mathbb{R}^3$. *J. Differ. Equations*, 177:419–453, 2001.

[37] W. Teka, J. Tabak, T. Vo, M. Wechselberger, and R. Bertram. The dynamics underlying pseudo-plateau bursting in a pituitary cell model. *J. Math. Neurosci.*, 1:1–12, 2011.

[38] M. R. Tinsley, I. Nkomo, and K. Showalter. Chimera and phase-cluster states in populations of coupled chemical oscillators. *Nature Phys.*, 8:662–665, 2012.

[39] N. Toporikova, J. Tabak, M. E. Freeman, and R. Bertram. A-type K^+ current can act as a trigger for bursting in the absence of a slow variable. *Neural Comput.*, 20:436–451, 2008.

[40] T. Vo and R. Bertram. Why pacing frequency affects the production of early afterdepolarizations in cardiomyocytes: An explanation revealed by slow-fast analysis of a minimal model. *Phys. Rev. E*, 99:052205, 2019.

[41] T. Vo, R. Bertram, J. Tabak, and M. Wechselberger. Mixed mode oscillations as a mechanism for pseudo-plateau bursting. *J. Comput. Neurosci.*, 28:443–458, 2010.

[42] T. Vo, R. Bertram, and M. Wechselberger. Bifurcations of canard-induced mixed mode oscillations in a pituitary lactotroph model. *Disc. Cont. Dyn. Syst.*, 32:2879–2912, 2012.

[43] M. Wechselberger. Existence and bifurcation of canards in $\mathbb{R}^3$ in the case of a folded node. *SIAM J. App. Dyn. Sys.*, 4:101–139, 2005.

[44] M. Wechselberger. Apropos canards. *T. Am. Math. Soc.*, 364:3289–3309, 2012.

[45] M. Wechselberger and G. J. Pettet. Folds, canards and shocks in advection-reaction-diffusion models. *Nonlinearity*, 23:1949–1969, 2010.

[46] J. Xie, H.-C. Kao, and E. Knobloch. Chimera states in systems of nonlocal nonidentical phase-coupled oscillators. *Phys. Rev. E*, 91:032918, 2015.